Icarus 253 (2015) 346–363

Contents lists available at ScienceDirect

Icarus

journal homepage: www.elsevier.com/locate/icarus

Geochemical terranes of Mercury's northern hemisphere as revealed by MESSENGER neutron measurements

Patrick N. Peplowski [a,*], David J. Lawrence [a], William C. Feldman [b], John O. Goldsten [a], David Bazell [a], Larry G. Evans [c], James W. Head [d], Larry R. Nittler [e], Sean C. Solomon [e,f], Shoshana Z. Weider [e]

[a] The Johns Hopkins University Applied Physics Laboratory, Laurel, MD 20723, USA
[b] Planetary Science Institute, Tucson, AZ 85719, USA
[c] Computer Sciences Corporation, Lanham-Seabrook, MD 20706, USA
[d] Department of Earth, Environmental and Planetary Sciences, Brown University, Providence, RI 02912, USA
[e] Department of Terrestrial Magnetism, Carnegie Institution of Washington, Washington, DC 20015, USA
[f] Lamont-Doherty Earth Observatory, Columbia University, Palisades, NY 10964, USA

ARTICLE INFO

Article history:
Received 22 September 2014
Revised 26 January 2015
Accepted 2 February 2015
Available online 14 February 2015

Keywords:
Mercury, surface
Spectroscopy
Terrestrial planets
Volcanism

ABSTRACT

The first map of variations in the abundances of thermal-neutron-absorbing elements across Mercury's surface has been derived from measurements made with the anti-coincidence shield on MESSENGER's Gamma-Ray Spectrometer (GRS). The results, which are limited to Mercury's northern hemisphere, permit the identification of four major geochemical terranes at the 1000-km horizontal scale. The chemical properties of these regions are characterized from knowledge of neutron production physics coupled with elemental abundance measurements acquired by MESSENGER's X-Ray Spectrometer (XRS) and GRS. The results indicate that the smooth plains interior to the Caloris basin have an elemental composition that is distinct from those of other volcanic plains units, suggesting that the parental magmas were partial melts from a chemically distinct portion of Mercury's mantle. Mercury's high-magnesium region, first recognized from XRS measurements, also contains high concentrations of unidentified neutron-absorbing elements. At latitudes north of ~65°N, there is a region of high neutron absorption that corresponds closely to areas known to be enhanced in the moderately volatile lithophile elements Na, K, and Cl, and which has distinctly low Mg/Si ratios. The boundaries of this terrane differ from those of the northern volcanic plains, which constitute the largest geological unit in this region.

1. Introduction

Measurements of Mercury's surface composition provide fundamental insights into the formation and evolution of the innermost planet. The MErcury Surface, Space ENvironment, GEochemistry, and Ranging (MESSENGER) spacecraft (Solomon et al., 2007) has been performing a detailed investigation of the geochemistry of Mercury's surface since orbit insertion on 18 March 2011. Key measurements are being acquired by MESSENGER's X-Ray Spectrometer (XRS) (Schlemm et al., 2007) and Gamma-Ray and Neutron Spectrometer (GRNS) (Goldsten et al., 2007). To date, data from these instruments have yielded elemental abundances for H, K, Th, and U, as well as elemental ratios by weight of Na/Si, Mg/Si, Al/Si, S/Si, Cl/Si, Ca/Si, Ti/Si, Cr/Si, Mn/Si, and Fe/Si (Nittler et al., 2011; Peplowski et al., 2011, 2012, 2014; Evans et al., 2012, 2014; Starr et al., 2012; Weider et al., 2012, 2014, 2015; Lawrence et al., 2013a). Spatially resolved measurements have been produced for a subset of these measurements, including H, Na/Si, Mg/Si, Al/Si, S/Si, Cl/Si, K, Ca/Si, Fe/Si, and Th. These results have confirmed the presence of an iron-poor crust, revealed that the surface is not depleted in moderately volatile elements (Na, K, Cl, and S), and demonstrated a geochemical diversity that is dominated by Mg-rich materials (Stockstill-Cahill et al., 2012).

The coverage, spatial resolution, and statistical precision of the MESSENGER surface composition measurements vary from element to element. This heterogeneity complicates a thorough understanding of the geochemical diversity of Mercury's surface and prompts a need for additional compositional observations and a synthesis of multiple datasets. We present an analysis of neutron measurements acquired with the anti-coincidence shield (ACS) on MESSENGER's Gamma-Ray Spectrometer (GRS), a portion of the GRNS instrument. With these measurements we examine the bulk concentrations and variability of neutron-absorbing

* Corresponding author.
E-mail address: Patrick.Peplowski@jhuapl.edu (P.N. Peplowski).

http://dx.doi.org/10.1016/j.icarus.2015.02.002
0019-1035/

elements across Mercury's surface. By combining these measurements with other MESSENGER datasets, we are able to define and characterize four major geochemical terranes in Mercury's northern hemisphere. This information provides a basis for examining the evolution of magmas erupted onto Mercury's surface, i.e., those that formed both its older, heavily cratered regions and younger volcanic plains.

2. Neutron measurements

2.1. Neutron production

Neutron spectroscopy is one of several techniques for investigating the chemical composition of a planetary surface. Neutron production on Mercury results from interactions initiated by galactic cosmic rays (GCRs), extra-solar particles (primarily protons) with energies ranging from <10 to >10,000 MeV/nucleon. GCRs constantly bombard Mercury's surface, penetrating to depths of a few meters and producing high-energy (E_n = ~1–100 MeV) neutrons via nuclear spallation. The portion of Mercury's near-surface volume sampled by measurements of these neutrons is hereafter referred to as the regolith for convenience, although it most likely also contains consolidated material.

The spallation neutron flux is proportional to the average atomic mass ($\langle A \rangle$) of the regolith (Gasnault et al., 2001). $\langle A \rangle$ is a bulk quantity that is calculated by summing over all of the elements comprising the regolith as

$$\langle A \rangle = \sum_i f_i A_i = \left[\sum_i \frac{w_i}{A_i} \right]^{-1}, \quad (1)$$

where f_i is the number fraction, A_i is the atomic mass, and w_i is the weight fraction for each element i. Spallation neutrons account for the highest-energy (>0.5 MeV) portion of the planetary neutron flux, an energy regime that is typically termed "fast neutrons." A portion of the fast neutron flux is moderated via scattering reactions within the regolith to lower (epithermal) energies of 0.5 eV to 0.5 MeV. The epithermal neutron flux is sensitive to the light-element content of the regolith, in particular H, as energy loss via scattering is inversely proportional to the mass of the scattering nuclei. Finally, a fraction of the epithermal neutron population is further down-scattered to very low (<0.5 eV) energies, where they reach thermal equilibrium with the surface.

In this thermal neutron regime, neutrons gain energy as efficiently as they lose it, and as a result a temperature-dependent Maxwellian distribution develops. The magnitude of this distribution increases until it reaches equilibrium with the rate of absorption and losses to space, making it an indicator of the total neutron absorption capacity of the regolith. This capacity is quantified by a parameter called the macroscopic neutron absorption cross section, Σ_a, a bulk quantity of the regolith that is calculated from the sum of the individual abundance-weighted microscopic thermal-neutron-absorption cross sections (σ_i) of each element i as

$$\Sigma_a = N_A \sum_i \left(\frac{w_i}{A_i} \right) \sigma_i, \quad (2)$$

where N_A is Avogadro's number (6.022×10^{23} atoms/mole) and σ_i is taken at a reference energy of 0.0253 eV from the Evaluated Nuclear Data File (ENDF VII), as given by Chadwick et al. (2011). The calculation is made under the assumption that all σ_i have an identical energy dependence inversely proportional to particle velocity. This assumption ignores the presence of cross-section resonances, a simplification that is justified by the close agreement between our σ_i values (Table 1) and those of Prettyman et al. (2013), who explicitly included all resonances. Following Elphic et al. (2000), Σ_a is expressed in units of 10^{-4} cm^2/g. When Σ_a is multiplied by the regolith density (g/cm^3), the product is proportional to the probability per unit path length that a thermal neutron will be absorbed.

2.2. Neutron measurements with the Gamma-Ray Spectrometer

This study uses neutron measurements from the anti-coincidence shield on the MESSENGER GRS. The ACS is a borated plastic (BC454) scintillator with a photomultiplier tube (PMT) readout. The primary function of the ACS is to act as an anti-coincidence detector to veto charged-particle (e.g., GCR) events in the GRS high-purity germanium (HPGe) gamma-ray sensor. The ACS is also sensitive to neutrons via the reaction

$$^{10}\mathrm{B} + n \rightarrow {}^{7}\mathrm{Li} + \alpha.$$

The ^{7}Li and α daughter products deposit their energy in the ACS, and those energies sum to the characteristic energy released by this particular neutron capture reaction. This sum manifests as a peak in the ACS spectra (Fig. 1), for which the total count rate is proportional to the neutron flux at the detector.

Because of the ACS geometry, which includes two optically connected but distinct sensor components, an annular cylinder and a thick disk (Goldsten et al., 2007), two separate neutron peaks are observed in the ACS spectra. The lower channel peak (peak 1 in Fig. 1a) is attributed to the top half of the sensor (the annulus), and the higher channel peak (peak 2 in Fig. 1a) is attributed to the bottom half of the sensor (the disk). The apparent energy (channel) difference is due to differences in the total light output measured by the PMT, as the disk is closer to the PMT and therefore has a higher effective light output than the annulus. That the lower channel peak originates from the annulus is supported by ground calibration measurements on the spacecraft-integrated instrument prior to launch. During that test, an AmBe neutron source was placed in the field of view of the annulus but outside the field of view of the disk. The measured spectrum had a single peak at the location of peak 1. Our analysis is limited to using the annulus-measured neutron events because of the higher signal-to-background of peak 1 (Fig. 1b).

Following the expected end of life of the HPGe cryocooler, which prohibited further acquisition of gamma-ray measurements, the GRS was repurposed via a flight software upgrade on 25 February 2013 to maximize the neutron measurement capabilities of the ACS. ACS neutron measurements are complementary to those of the MESSENGER Neutron Spectrometer (NS; Goldsten et al., 2007). The ACS is situated on the main instrument (+z in spacecraft-fixed Cartesian coordinates; Leary et al., 2007) deck of the spacecraft, which generally faces the planet at low altitudes. This placement contrasts with that of the NS, which is located on the anti-sunward (+y) deck and has a highly variable view of Mercury's surface. As a result, the ACS measurements are subject to smaller systematic variability than is observed in the NS measurements (e.g., Lawrence et al., 2013a). Unlike the NS, which has the capability to segregate the thermal, epithermal, and fast neutron signals, the ACS observations provide a single measure that includes contributions from all three neutron-energy bands.

2.3. Composition information from ACS measurements

Our inability to differentiate between thermal, epithermal, and fast neutrons with the ACS measurements complicates the use of this dataset to derive surface composition information. This situation is partially analogous to Lunar Prospector (LP) "moderated neutron" measurements (Genetay et al., 2003), which were also derived from a BC454 anti-coincidence shield. Unlike the

Table 1
Model surface compositions used in radiation transport modeling.

	Z	A (amu)	σ_a[a] (barns)	Model composition[b] (wt%)						
				F1	P1	F2	P2	P3	F3	P4
O	8	15.99	1.91×10^{-4}	46.4	48.55	43.6	40.73	44.96	43.5	48.15
Na	11	22.99	0.528	3.2	1.52	0.40	2.37	2.61	3.2	5.32
Mg	12	24.31	0.063	9.1	6.35	13.9	19.66	12.28	9.1	5.60
Al	13	26.98	0.234	7.0	9.03	5.4	2.84	6.53	7.0	3.36
Si	14	28.09	0.165	27.5	28.32	24.2	23.68	26.13	25.1	27.99
S	16	32.06	0.514	1.6	1.41	2.2	3.08	1.83	1.6	2.52
Cl	17	35.45	33.2	–	0.05	–	0.12	0.13	–	0.42
K	19	39.10	2.06	0.5	0.04	0.2	0.03	0.04	0.5	0.18
Ca	20	40.08	0.436	4.2	3.67	4.6	5.57	3.40	4.2	5.32
Ti	22	47.87	5.99	0.2	0.34	0.2	0.28	0.31	0.2	0.34
Cr	24	52.00	3.04	–	0.14	–	0.12	0.13	–	0.14
Mn	25	54.94	13.4	–	0.11	–	0.09	0.10	–	0.11
Fe	26	55.85	2.56	0.7	0.56	0.9	1.42	1.57	6.3	0.56
Th	90	232.04	7.34	–	1.26×10^{-5}	–	1.24×10^{-5}	1.25×10^{-5}	–	1.23×10^{-5}
U	92	238.03	3.38[c]	–	9.11×10^{-6}	–	8.96×10^{-6}	9.03×10^{-6}	–	8.87×10^{-6}
		$\langle A \rangle$ (amu)[d]		20.7	20.57	21.0	21.36	20.90	21.5	20.65
		Σ_a (10^{-4} cm^2/g)[d]		27.0	30.86	31.0	37.57	38.37	41.5	56.14

[a] Calculated from isotope-specific $\sigma(n,\gamma)$ values at 0.0253 eV from Chadwick et al. (2011) and standard (terrestrial) isotopic abundances. Units are barns, where 1 barn = 10^{-24} cm^2.
[b] "F" models were subject to full-mission radiation transport simulations (see Section A.2). "P" models were subject to partial simulations (modeled neutron fluxes convolved with the ACS detector response; see Section 2.3). Models are ordered in the table by increasing values of Σ_a.
[c] U has large neutron-induced fission cross sections that increase its effective absorption but are not listed here.
[d] $\langle A \rangle$ and Σ_a values are from Eqs. (1) and (2), respectively.

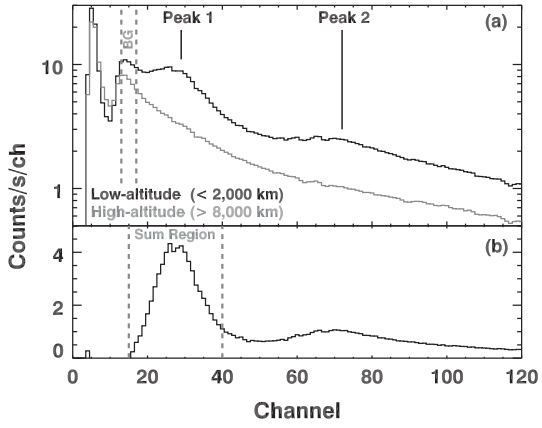

Fig. 1. Example energy deposition spectra from the GRS anti-coincidence shield. (a) Summed spectra at low (black) and high (gray) altitudes. The two neutron capture peaks are labeled, as is the spectral region used for background (BG) normalization. (b) The residual spectrum after subtracting the high-altitude spectrum, scaled to the BG region, from the low-altitude measurements.

MESSENGER ACS, the LP ACS had the capability to electronically isolate fast neutron events, limiting its measurements to thermal and epithermal contributions. The LP moderated-neutron measurements were interpreted in the context of global maps of thermal, epithermal, and fast neutrons (Maurice et al., 2004), which led to the conclusion that the signal was dominated by lunar epithermal neutrons, with smaller contributions from thermal neutrons (Genetay et al., 2003).

Maps of thermal, epithermal, and fast neutron count rates have not been produced for Mercury, so the MESSENGER ACS measurements cannot be interpreted in the context of existing neutron data. Instead we rely on simulations of neutron production and detection to interpret the ACS data with respect to Mercury's surface composition. Our radiation transport modeling toolkits include the MCNPX code (Pelowitz, 2005), which has an extensive history of application to the analysis of neutron and gamma-ray spectroscopy datasets (e.g., McKinney et al., 2006; Prettyman et al., 2006, 2012, 2013; Kim et al., 2006; Evans et al., 2012; Lawrence et al., 2010, 2013a), and GEANT4 (Agostinelli, 2003), which has previously been used to model MESSENGER detector response functions (Peplowski et al., 2012). The GEANT4-modeled energy-dependent response of the ACS to neutrons is shown in Fig. 2a.

We used MCNPX to simulate GCR-induced neutron production on Mercury for seven model surface compositions loosely based on the MESSENGER-derived Mercury surface compositions of Nittler et al. (2011), Peplowski et al. (2011, 2012, 2014), Weider et al. (2012, 2014, 2015), and Evans et al. (2012, 2014). Those results, which were typically reported as abundance values relative to Si, were converted to absolute abundances with the assumption

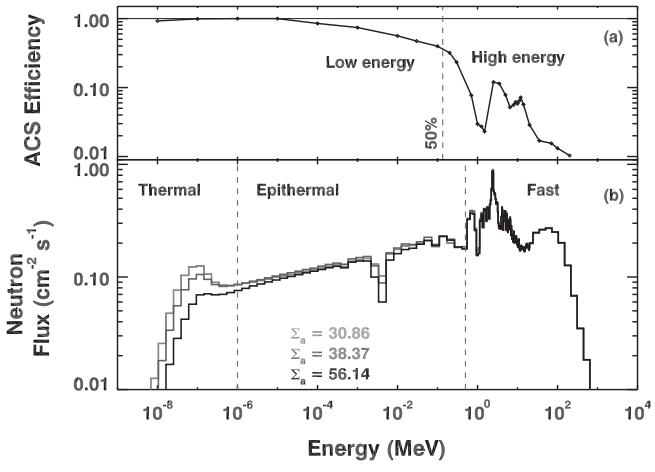

Fig. 2. (a) Modeled energy dependent neutron detection efficiency for the GRS ACS. Half of the ACS-measured neutrons have energies below 0.135 MeV (vertical dashed line), a region that is termed the low-energy regime. Likewise, 50% of the measured neutrons have energies above 0.135 MeV, and this energy range is termed the high-energy regime. (b) Modeled neutron fluxes for three hydrogen-free Mercury surface compositions (P1, P3, and P4 of Table 1) with macroscopic neutron absorption cross sections (Σ_a, in units of 10^{-4} cm^2/g) that span the range of compositions in Table 2. The typical neutron energy regimes of interest—thermal, epithermal, and fast—are noted.

O/Si = 1.72 (a mean value for Solar System materials) and by solving for the Si abundance required to obtain a sum of 100 wt%. The values of A_i, σ_i, and w_i for each element of interest as well as the bulk quantities $\langle A \rangle$ and Σ_a are given for each model composition in Table 1. Some of those compositions were chosen to depart from average MESSENGER measurements to ensure that the full range of Σ_a values of interest for Mercury were considered in our simulations. The models are labeled by the simulation type corresponding to each composition. Compositions F1–F3 are models that were subjected to full mission simulation, whereas compositions P1–P4 are models that were subject to partial simulations. The full simulations represent modeling of the ACS count rates on a spectrum-by-spectrum basis, the details of which are given in Appendix A. The partial simulations were subjected only to full-planet simulations of the GCR-induced neutron flux at the surface. The simulated neutron fluxes for models P1, P3, and P4 are shown in Fig. 2b. Note that these compositions have hydrogen concentrations of 0 ppm. Fig. 2b also denotes typical partitioning among thermal, epithermal, and fast neutrons for comparison with the energy sensitive measurements of the NS.

For the model compositions that did not undergo full-mission simulations (P1–P4), we convolved the simulated neutron fluxes with the energy-dependent response of the ACS to estimate the sensitivity of the GRS neutron measurements to varying surface compositions. For a modeled composition similar to Mercury's mean elemental concentrations (P3; Table 1), 50% of the ACS-measured neutrons have energies less than 0.135 MeV. We label this energy band (10^{-8}–0.135 MeV) the "low-energy" neutron regime and note that it encompasses the entire thermal and most of the epithermal neutron bands (see Fig. 2). The remaining 50% of the ACS sensitivity range (>0.135 MeV) is denoted the "high-energy" neutron regime and generally corresponds to the fast neutron energy band (Fig. 2). Although the ACS does not discriminate between low- and high-energy neutrons, this delineation is nonetheless useful for interpreting the ACS measurements. This point is illustrated in Fig. 2b, which shows that the modeled differences among MESSENGER-derived Mercury surface compositions are contained entirely within the low-energy neutron regime. This inference was verified by comparing summed, ACS-response-weighted planetary neutron fluxes for all seven model surface compositions (Table 1) to their $\langle A \rangle$ and Σ_a values. These comparisons yield correlation coefficients of −0.98 for ACS counts versus Σ_a, and 0.36 for ACS counts versus $\langle A \rangle$. This result indicates that, in the limit of low and invariant H concentrations, ACS measurements are strongly correlated with variations in thermal neutrons and, by extension, Σ_a across Mercury's surface.

The ACS measurements are also sensitive to the epithermal neutron flux, which is known to be a function of the H content of the regolith. Fig. 3 shows modeled neutron fluxes for a composition similar to that found in Mercury's high northern latitudes (P4; Table 1) as a function of varying H content. These neutron fluxes are multiplied by the ACS response (Fig. 2a) and plotted as a function of H content in Fig. 4. Interpreting the magnitude of H contributions to our ACS neutron measurements requires an estimate of the H content of Mercury's surface. On the basis of neutron spectrometry (Lawrence et al., 2013a), surface reflectance (Neumann et al., 2013), and thermal modeling with measured topography (Paige et al., 2013), Mercury's polar deposits as imaged by Earth-based radar (Slade et al., 1992; Harmon et al., 2011) are likely to be dominated by water ice. We therefore adopted a simple H distribution with 100 wt% H_2O, exposed at the surface, in all of the radar-bright polar deposits imaged by Earth-based radar and 50 ppm H elsewhere. The estimate of 50 ppm H in surface material other than polar deposits accounts for solar-wind-implanted H and is comparable to measured values for the lunar highlands

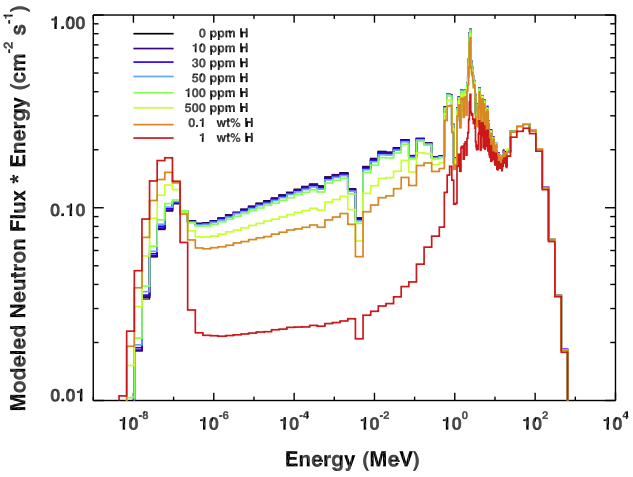

Fig. 3. Modeled neutron fluxes for Mercury's northern composition (P4, Table 1) with eight hypothetical H concentrations.

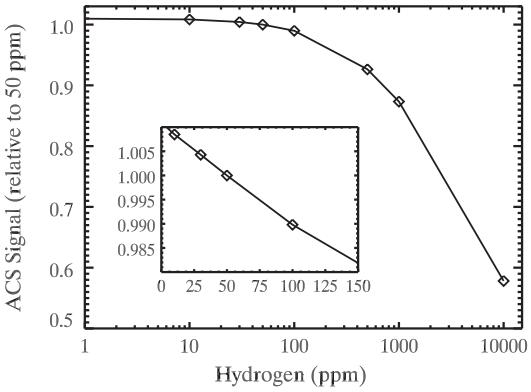

Fig. 4. Simulated ACS signal intensity as a function of H content. The signal intensity is derived from the sum of the product of the modeled ACS response (Fig. 2a) and our modeled neutron fluxes (Fig. 3). The results are normalized to 50 ppm H, the assumed hydrogen concentration outside of the polar deposits (Section 2.3).

(~5–150 ppm; Haskin and Warren, 1991; Lawrence et al., 2015). The value of 50 ppm for the H abundance outside of polar deposits was also assumed for the gamma-ray production model of Evans et al. (2012), who used gamma rays from both neutron inelastic scattering and neutron capture reactions to derive surface abundances of S, Ca, and Fe on Mercury. In each case, the elemental concentrations derived from the two mechanisms agreed to within one standard deviation. Had the hydrogen concentration been significantly different from 50 ppm, the elemental concentrations derived from the two reaction mechanisms would not have been in agreement.

Following the methodology of Peplowski et al. (2014), our model H distribution was convolved with the altitude-dependent spatial response of the ACS measurements to derive the effective H distribution observed by the ACS. The result is a mean value of ~95 ppm at high northern latitudes (>78°N) and 50 ppm elsewhere. From Fig. 4, we see that this scenario corresponds to a small (~1%) but notable decrease in the predicted ACS signal over the polar region (95 ppm H) relative to the equatorial region (50 ppm H). This prediction is based on our assumed H distribution, specifically the assumption that all polar deposits consist of 100% H_2O exposed at the surface. Both the radar data and MESSENGER NS measurements support the presence of a layer of H-poor material

(12–47 g/cm^2 thick; Lawrence et al., 2013a) overlying the water ice in most polar deposits. This layer, which is comparable in thickness to the depth sensitivity of the thermal and epithermal measurements, would lower the sensitivity of the ACS to the polar H deposits. Measurements of surface reflectivity with MESSENGER's Mercury Laser Altimeter (Neumann et al., 2013) and Mercury Dual Imaging System (Chabot et al., 2014) indicate that most radar-bright polar deposits show evidence for burial by material darker than Mercury's average surface, whereas in those at the highest northern latitudes display reflectance values consistent with ice exposed at the surface. The evidence for burial of some of the deposits suggests that contributions from H to the ACS count rates may be less than the 1% predicted here. Regardless, the effects of H on the ACS measurements are limited to high latitudes (>78°N), unless the assumption of low, near-uniform H in non-polar regions is invalid. We discuss the issue of the influence of H concentrations on the ACS measurements further in Section 5.2.

3. Data reduction procedure

3.1. Dataset

This analysis is of GRS/ACS data obtained from 1 March 2013 to 28 February 2014. The data include ACS energy deposition spectra (e.g., Fig. 1) acquired with integration times of 20 and 1800 s. Shorter integration times correspond to measurements acquired at low (<4000 km) altitudes. Spacecraft ephemeris and detector housekeeping data accompany each spectrum. NS triple-coincidence counter measurements are appended to the ACS dataset, as they provide a proxy for monitoring the local GCR flux (Feldman et al., 2010; Lawrence et al., 2013a). The NS data were interpolated to the time cadence of the ACS measurements.

Data acquired during solar energetic particle (SEP) events were removed prior to analysis, which eliminated 14.1% of the total dataset. Removal of SEP-contaminated data was necessary given that SEPs compromise the ACS spectra and the use of the NS triple-coincidence counter as a GCR proxy. Spectra acquired during energetic electron events (EEEs; Lawrence et al., 2013b) were likewise removed, as they modify the ACS spectral continuum and complicate the derivation of neutron count rates. Removal of EEEs typically resulted in the loss of just a few spectra per orbit, when they were present.

3.2. Neutron count rate derivation

The total peak count rates for each ACS spectrum (Fig. 1) are directly proportional to the neutron flux at the detector. Deriving neutron count rates from these peaks requires determination of the background-free peak areas and correction for the live time of each spectrum. This process is complicated by the presence of a time- and altitude-varying continuum, which originates from gamma rays emitted by the spacecraft and Mercury, as well as GCR energy deposition in the ACS. We leveraged MESSENGER's highly eccentric orbit about Mercury (8-h orbital period) to provide orbit-by-orbit measurements of the detector backgrounds using spectra acquired at high (>8000 km) altitudes. The high-altitude data are acquired too far from Mercury to contain an appreciable signal from the planet, as indicated by the absence of neutron peaks in the spectra (Fig. 1a). These measurements therefore provide regular sampling of the local backgrounds in the detector. High-altitude spectra were summed by orbit to maximize the statistics of the background characterization while simultaneously limiting the introduction of time-dependent variability.

Neutron count rates were derived from the low-altitude (<2000 km altitude) spectra by first removing the background contributions from each measurement. For each low-altitude spectrum, the corresponding (same orbit) high-altitude summed spectrum was normalized to the low-altitude continuum in the background (BG) region shown in Fig. 1a. The normalized background was subtracted from the low-altitude spectrum, and the resulting residual is dominated by the neutron peaks of interest (Fig. 1b). The sum of the residual events within the peak channel range of interest defines the number of measured neutron events for each spectrum. Temperature-induced gain shifts, which move the neutron peak relative to our fixed-peak sum region (Fig. 1b), can alter the derived neutron peak event values. Using the co-located GRS preamplifier temperature sensor as a stand-in for the temperature of the ACS, we empirically removed the small temperature-induced variability in the peak areas on a spectrum-by-spectrum basis by normalizing to an acquisition temperature of −7.5 °C.

Finally, we derived neutron count rates by correcting each measurement for the accumulation time t_s and detector dead time fraction (F_D) for each spectrum. This correction takes the form $(1-F_D)^{-1}$, where F_D is calculated from the onboard dead time counter (DTC) as

$$F_D = 16\times10^{-6}\left(\frac{DTC}{t_s}\right). \quad (3)$$

For low-altitude measurements, t_s is 20 s and F_D is typically ~7%. This process was repeated for each low-altitude spectrum to produce a time series of the neutron count rate, $C_n(t)$, which serves as the basis for this analysis.

3.3. Data reduction

The constantly changing altitude and attitude of the MESSENGER spacecraft dominates the observed variability in $C_n(t)$. This phenomenon is illustrated in Fig. 5, which highlights ACS measurements from two example orbits. Both examples include modeled ACS neutron count rates for comparison. The modeled count rates, which are discussed in detail in Appendix A, were derived from simulations that account for the generation of neutrons by GCR-induced spallation reactions within the regolith, their transport through the regolith to the surface, their transport from the surface to the spacecraft, interactions with spacecraft materials, and detection by the ACS. The model is produced on a spectrum-by-spectrum basis, and the result is a time series of modeled ACS neutron count rate that is directly comparable to the ACS measurements. Models are generated for a range of hypothetical regolith compositions (Table 1), and two examples (F1, F3) with different macroscopic neutron absorption cross sections (41.6 and 27.1 × 10^{-4} cm^2/g) are plotted in Fig. 5.

The strong dependence of $C_n(t)$ on the spacecraft altitude is seen in Fig. 5a. Fig. 5b shows second-order variability associated with non-isotropic detector response, as a sharp decrease in $C_n(t)$, in both measurements and the model, is coincident with a sudden change in the orientation of the GRS relative to Mercury, particularly in θ, the angle between the detector boresight direction and the nadir direction (see Appendix A). The increase in θ corresponds to off-pointing of the ACS from Mercury, and the result is lower sensitivity to neutrons from Mercury. The modeled count rates reproduce the altitude- and attitude-dependent behavior of the measurements, providing confidence in the fidelity of the models. The models highlight the inverse relationship between Σ_a and $C_n(t)$, as the higher-Σ_a (41.6 × 10^{-4} cm^2/g) model produces a lower neutron count rate than the lower-Σ_a (27.1 × 10^{-4} cm^2/g) composition.

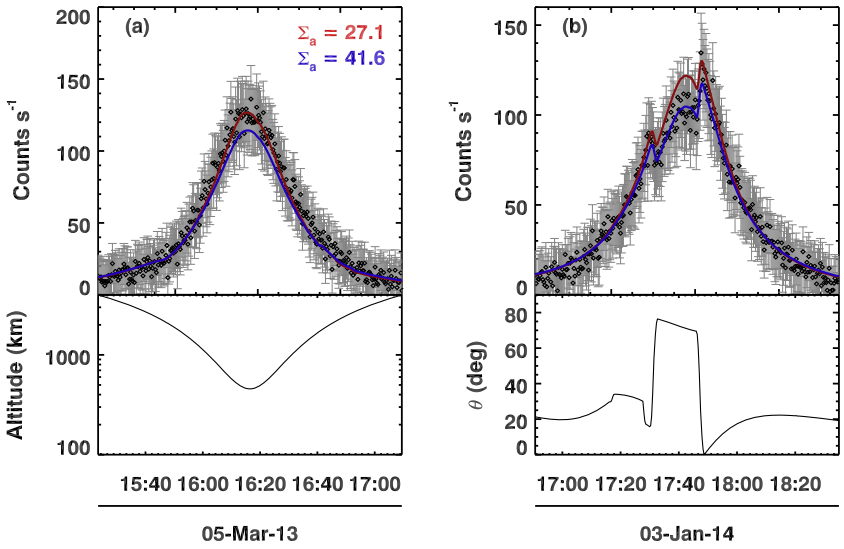

Fig. 5. Comparison of measured (black diamonds, gray error bars) and simulated (color curves) neutron count rates for typical measurements taken on (a) 5 March 2013 and (b) 3 January 2014. Times are in UTC. Simulated count rates are derived for model compositions F1 and F3 (Table 1). Comparisons of the count rates with (a) spacecraft altitude and (b) detector orientation, represented by the angle θ, highlight the dependence of the measured count rates on spacecraft altitude and attitude. Σ_a values (color) are shown in units of 10^{-4} cm^2/g.

The systematic variability present in the neutron count rate measurements masks signatures of compositional variability on Mercury's surface. To remove these systematic dependencies, $C_n(t)$ was normalized to a reference viewing geometry of $\theta = 0°$, an altitude of 1000 km, a vertical velocity of 0 km/s, and a triple coincidence counter rate of 26.5 counts s^{-1}. This process is analogous to the use of photometric corrections to normalize global images taken at a variety of incidence, emission, and phase angles to a standard viewing geometry. Our normalization procedure is discussed in detail in Appendix A.

4. Results

4.1. Neutron count-rate map

The neutron count-rate time series, corrected for viewing geometry for both the measurements and the model, was mapped across Mercury's surface in 5° × 5° pixels. For each pixel, the total neutron count rate was tallied and divided by the number of samples to derive the mean count rate for that pixel. The tally was limited to measurements that met a set of selection criteria that included acquisition at altitudes <1600 km and $\theta < 45°$. These restrictions removed the least-sensitive measurements from the dataset, thereby reducing the statistical and systematic uncertainties of the mapped count rates. We also removed a small number of measurements acquired during periods of outlying triple-coincidence measurements, as those intervals may have been coincident with small solar particle events not removed from the dataset during the initial selection (Section 3.1). The remaining dataset provides 30–150 measurements per pixel, with higher values generally found at higher latitudes. The per-pixel statistical uncertainties are <1%. MESSENGER's eccentric orbit, coupled with the 1600 km altitude cutoff, limit the coverage of the neutron count rate map to latitudes poleward of 20°N.

The normalization of the data to the reference viewing geometry (Appendix A) had the objective of removing all systematic variations from the modeled and measured neutron time series. The model, which was derived for uniform Mercury surface compositions, should therefore display a uniform count-rate map. The model map shows small but non-zero variations (standard deviation of 0.6%), suggesting that minor systematic variations were not removed during the normalization procedure. This variability is two orders of magnitude smaller than that observed in the uncorrected modeled count rates, which ranged from ~0 to ~200 counts s^{-1} (e.g., Fig. 5). The variability in the model map is much smaller than that observed in the measurement map, which exhibits a full-range variation of 8.6%. The variations in the measurement map are therefore indicative of a signature of compositional heterogeneity that is an order of magnitude larger than the residual systematic variability (0.6%) exhibited in the model map. To eliminate any contributions from the remaining systematic variability to our final neutron count rate map, we empirically removed the variations in the model map from the measurement map.

The resulting map of measured neutron count rates was smoothed over a moving circular window with a radius of 650 km, which corresponds to the approximate average spatial resolution of the ACS measurements. Note that the actual spatial resolution of the ACS measurements, for which the full-width half maximum can be approximated by the orbital altitude multiplied by a factor of 1.5, varies greatly over the mapped ACS data (altitudes of 250–1600 km). The smoothed map was re-binned to the 5° × 5° base map resolution. Unlike the original pixels, which were equal in degree size, the re-binned pixels were resized so that they are equal in area. The resulting neutron count rate map is shown in Fig. 6. The per pixel statistical uncertainties of the smoothed map are expected to be better than the <1% per pixel uncertainties of the unsmoothed map.

4.2. Σ_a map

The smoothed neutron count-rate map (Fig. 6) displays a full-range variation of 3.2% across the mapped portion of Mercury's surface. Regions with lower count rates are observed over Mercury's north polar region, as well as at mid-latitudes between approximately −135° and −45°E longitude. The highest count rate is observed in an area between 20° and 60°N, and between 135° and −170°E. To derive chemical information regarding Mercury's regolith from the neutron count-rate map (Fig. 6), it is necessary to convert these measurements to a physical quantity related to

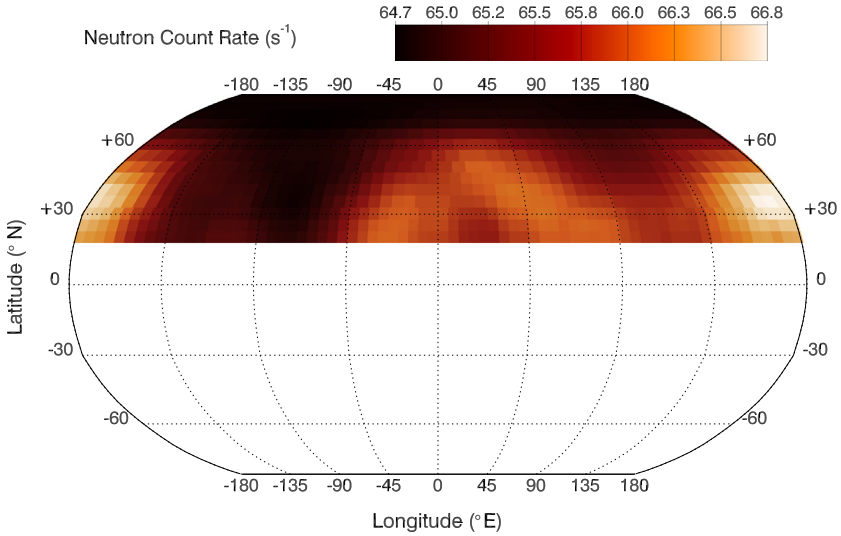

Fig. 6. Neutron count rates across Mercury's mid to high northern latitudes, derived from GRS/ACS data and normalized to the reference viewing geometry (Section 3.3). Regions south of 20°N are unmapped.

surface composition. In Section 2.3, we argued that the ACS measurements are predominantly sensitive to Σ_a (Eq. (2)) in low-H regions, or Σ_a plus H content in high-latitude (>78°N) regions. For the remainder of this analysis, we assume that all variations in neutron count rates are due to Σ_a. In Section 5.2 we discuss further the measurements in the polar region, where the H content is important, including the possible contributions from H.

Measurements of Σ_a have long been used to characterize the geochemical diversity of planetary surfaces. On the Moon, thermal neutron measurements provide maps that can be used to discriminate between anorthositic and mafic chemistries (Feldman et al., 2000). Lunar Σ_a measurements were used to map the distribution of KREEP (material rich in K, rare earth elements, and P), which led to the derivation of global abundance maps for the rare earth elements Gd and Sm (Elphic et al., 2000). On asteroid 4 Vesta, thermal-neutron-derived Σ_a maps were used to map the distribution and concentration of eucritic material across the surface (Prettyman et al., 2013). The analyses for the Moon and Vesta were facilitated by large sets of rock and soil samples, i.e., Apollo lunar samples and howardite–eucrite–diogenite meteorites, respectively. The relationship between thermal neutron measurements and Σ_a was derived from radiation transport modeling of the elemental compositions of these samples (Elphic et al., 2000; Prettyman et al., 2013).

In the absence of samples from Mercury, we used the model surface compositions of Table 1 as input to the radiation transport simulations. Three of the compositions (F1–F3) were subject to full-mission simulations that were normalized to the ACS measurements (see Appendix A). Four of the compositions (P1–P4) were subject to partial simulation, consisting of modeled surface neutron fluxes (e.g., Fig. 2b) convolved with the response of the ACS (Fig. 2a). The partial simulations were normalized to the full-mission simulations using compositions F2 and P1, which had virtually identical Σ_a values. The model results were used to define a relationship between ACS-measured count rates and Σ_a. This relationship, shown in Fig. 7, was used to derive the Σ_a map shown in Fig. 8.

4.3. Σ_a normalization

The relationship (Fig. 7) used to convert our neutron count rate map to the Σ_a map was derived from modeled count rates, which

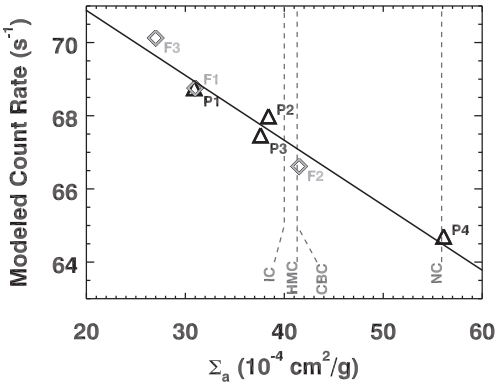

Fig. 7. Modeled relationship between ACS neutron count rates and the macroscopic neutron absorption cross section Σ_a (in units of 10^{-4} cm^2/g). Models include full-mission simulations (gray diamonds, F1–F3 of Table 1) and partial simulations (black triangles; P1–P4 of Table 1). The Σ_a values of the reference Mercury surface compositions (Table 2) are marked by vertical dashed lines for comparison with the modeled compositions.

themselves were subject to an overall normalization to the dataset (Appendix A). This normalization included an implicit assumption regarding the average Σ_a value for Mercury's surface. As a result there may be a constant offset in the relationship between neutron count rates and Σ_a that is not represented in Fig. 7. In acknowledgment of this possibility, we report two sets of values for the Σ_a map (Fig. 8). The first set of values, $\delta\Sigma_a$, are the relative variability of Σ_a across the mapped region about a mean value, Σ_a^0. This unspecified value for Σ_a^0 accounts for the uncertainty in the absolute calibration of the models. The second set of reported Σ_a values corresponds to a "best guess" for the absolute calibration made on the basis of independent MESSENGER measurements. These values were derived from an additional set of Mercury surface compositions (Table 2) that were more closely aligned with MESSENGER XRS and GRS measurements (Evans et al., 2012, 2014; Nittler et al., 2011; Peplowski et al., 2011, 2012, 2014; Weider et al., 2012, 2014, 2015). The four compositions include a Caloris basin interior plains composition (CBC), a northern composition (NC), a high-magnesium region (Weider et al., 2015) composition (HMC), and an intermediate composition (IC). The Σ_a values for these

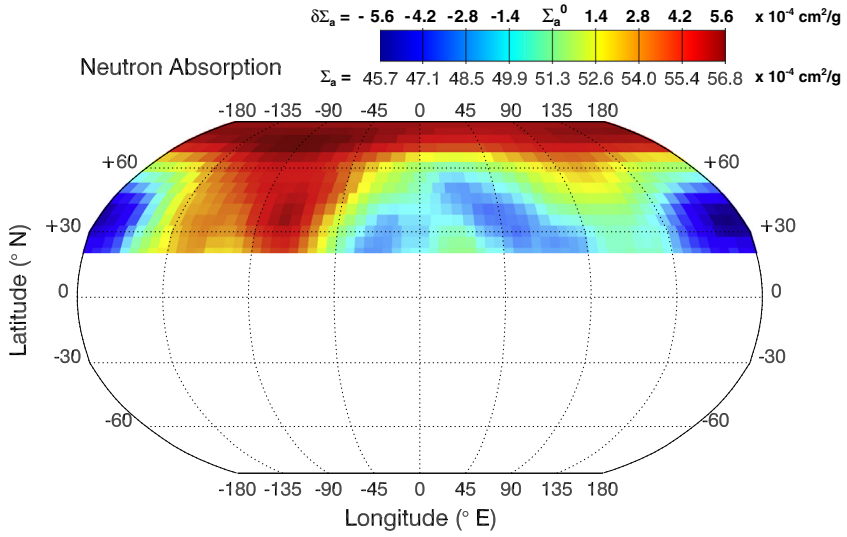

Fig. 8. Macroscopic neutron absorption cross section (Σ_a) over Mercury's northern hemisphere. The color bar indicates both the relative variability in Σ_a ($\delta\Sigma_a$) observed over the surface (top scale values) and the best-guess absolute calibration (bottom scale values), under the assumption that $\Sigma_a^0 = 51.3 \times 10^{-4}$ cm^2/g (see Section 4.3). Regions in white are unmapped.

Table 2
MESSENGER-derived Mercury surface compositions.

	Z	A (amu)	σ_a[a] (barns)	Model compositions (wt%)				Contribution to Σ_a (%)[b]
				IC	NC	HMC	CBC	
O	8	15.99	1.91×10^{-4}	44.12	47.21	40.99	46.78	0.07
Na	11	22.99	0.528	2.57	5.22	2.38	2.72	9.94
Mg	12	24.31	0.063	12.06	6.86	17.87	7.62	3.87
Al	13	26.98	0.234	7.44	5.76	2.38	8.98	7.64
Si	14	28.09	0.165	25.65	27.45	23.83	27.20	20.55
S	16	32.06	0.514	1.80	1.92	2.62	1.36	4.15
Cl	17	35.45	33.2	0.13	0.41	0.12	0.14	24.96
K	19	39.10	2.06	0.04	0.18	0.04	0.04	0.50
Ca	20	40.08	0.436	4.10	3.84	5.24	4.08	6.31
Ti	22	47.87	5.99	0.31	0.33	0.29	0.33	5.25
Cr	24	52.00	3.04	0.13	0.14	0.12	0.14	1.02
Mn	25	54.94	13.4	0.10	0.11	0.10	0.11	3.41
Fe	26	55.85	2.56	1.54	0.55	2.38	0.54	7.72
Sm[c]	62	150.36	10,100	8.6×10^{-5}	7.3×10^{-5}	8.6×10^{-5}	2.8×10^{-4}	1.18
Gd[c]	64	157.25	22,800	1.6×10^{-4}	9.7×10^{-5}	1.2×10^{-4}	3.7×10^{-4}	3.40
Th	90	232.04	7.34	1.7×10^{-5}	1.4×10^{-5}	1.7×10^{-5}	5.4×10^{-5}	0
U	92	238.03	3.38[d]	9.0×10^{-6}	9.0×10^{-6}	9.0×10^{-8}	9.0×10^{-6}	0
		$\langle A \rangle$ (amu)[e]		21.03	20.64	21.42	20.72	
		Σ_a (10^{-4} cm^2/g)[e]		40.0	55.9	41.3	41.3	

[a] Calculated from isotope-specific $\sigma(n,\gamma)$ values at 0.0253 eV from Chadwick et al. (2011) and standard (terrestrial) isotopic abundances. Units are barns, where 1 barn = 10^{-24} cm^2. $\sigma(n,\gamma)$ values for Gd and Sm are from Prettyman et al. (2013).
[b] Calculated from the contribution of each element, averaged over the four compositions, to the total Σ_a value calculated from the average composition.
[c] Estimated with chondritic Th/Sm and Th/Gd weight ratios of 0.195 and 0.146, respectively, as derived from Lodders and Fegley (1998).
[d] U has large neutron-induced fission cross sections that increase its effective absorption but are not listed here.
[e] $\langle A \rangle$ and Σ_a values are from Eqs. (1) and (2), respectively.

compositions are noted in Fig. 7, which shows that our earlier modeled compositions likely span the full Σ_a regime of interest for Mercury.

The Mercury surface compositions listed in Table 2 were derived from spatially resolved measurements of chemical composition where possible, i.e., for Mg, Al, S, K, and Ca (Weider et al., 2012, 2015; Peplowski et al., 2012). Where available, spatially resolved Fe and Th data were also used, but otherwise the mean northern hemisphere value was adopted. For Cl and Na (Peplowski et al., 2014; Evans et al., 2014), we used the high-northern-latitude abundances for the NC and the equatorial abundances for the CBC, IC, and HMC. The abundances of some neutron absorbers, such as Mn and Cr, are not well characterized, so we used the mean Cr/Si and Mn/Si values of Weider et al. (2014). For all regions we used the northern-hemisphere-average U concentration (Peplowski et al., 2011). Gd and Sm are two important neutron-absorbing elements that are not directly measured by MESSENGER. We estimated their concentrations on Mercury by combining regional Th values (Peplowski et al., 2012) with chondritic Th/Sm (0.195) and Th/Gd (0.146) weight ratios (Lodders and Fegley, 1998).

The mean contributions of each individual element to the total Σ_a value are indicated in Table 2. These values show that contributions from Cl, Si, and Na dominate Σ_a on Mercury, followed by Fe, Al, and Ca. Because Si is known to vary by $\leqslant$15% at the 100-km horizontal scale in Mercury's northern hemisphere (Peplowski et al., 2012), whereas Cl/Si and Na/Si vary by at least a factor of two (Evans et al., 2014; Peplowski et al., 2014), we

expect that variations in Cl and Na will largely dominate variations in Σ_a. This conclusion may not hold for all regions, however. For example, the low Fe content of the CBC (0.6 wt%) compared with that of the HMC (2.4 wt%) is a major contributor to the observed difference in Σ_a between these regions.

The best-guess Σ_a values are derived from constraints on Σ_a^0 provided by the compositions listed in Table 2, as well as from the neutron absorption measurements made during MESSENGER's Mercury flybys (Lawrence et al., 2010). The compositions shown in Table 2 produce only lower limits on actual Σ_a values, given that they may omit contributions for some neutron absorbers. These constraints are as follows: (1) Σ_a must be at least 41.3×10^{-4} cm^2/g in the Caloris basin, (2) Σ_a must be at least 55.9×10^{-4} cm^2/g at high northern latitudes (>70°N; NC composition of Table 2), and (3) NS measurements made during the three Mercury flybys (Lawrence et al., 2010) indicate that the average Σ_a of the surface is at least 45×10^{-4} cm^2/g. We treat (3) as a loose constraint, given that the area sampled by the NS during the flybys only partially overlaps our mapped regions. A Σ_a^0 value of $\geqslant 51.3 \times 10^{-4}$ cm^2/g is required to satisfy all three constraints, specifically constraint (2). We therefore adopted this Σ_a^0 value to derive the best-guess calibration (Fig. 8). We note, however, that higher Σ_a^0 values are also possible if our modeled compositions underestimate the abundances of, or omit one or more, neutron-absorbing elements. As a result, the $\delta\Sigma_a$ values are more robust than the absolute values reported for Σ_a.

5. Mercury's major geochemical terranes

The presence of large, contiguous geochemical terranes in Mercury's northern hemisphere at the ~1000-km horizontal resolution of the ACS measurements is indicated by the Σ_a maps (Figs. 8 and 9). The lowest Σ_a values are found in an area with a boundary that closely matches the outline of the Caloris basin interior smooth plains (Fig. 9a), although the Σ_a-low extends somewhat beyond the northeastern boundary of Caloris. The north polar region (latitudes >65°N) also appears to be a continuous unit, and it exhibits the highest Σ_a values measured. Both of these regions have also been identified as compositionally distinct on the basis of major-element (e.g., Mg/Si, Al/Si, Fe/Si) measurements (Weider et al., 2015). Similarly, the moderately high Σ_a values observed at mid-equatorial latitudes between −60° and −105°E are spatially coincident with the highest Mg/Si values observed on Mercury's surface (Fig. 9b; Weider et al., 2015).

A comparison of the ACS-derived Σ_a map to the NS flyby measurements of Lawrence et al. (2010) is also useful. The Lawrence et al. (2010) analysis yielded Σ_a values and two-standard-deviation errors of $\sim(60 \pm 10) \times 10^{-4}$ cm^2/g and $\sim(45 \pm 15) \times 10^{-4}$ cm^2/g for

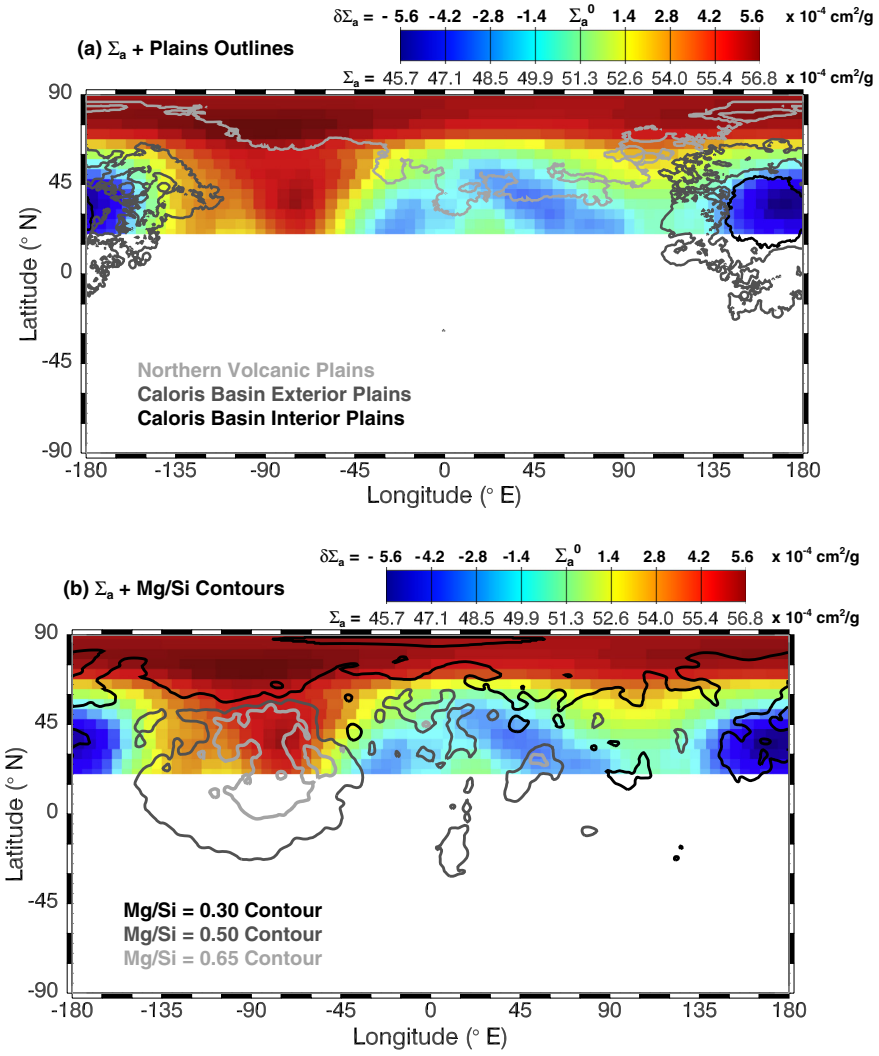

Fig. 9. (a) Map of Σ_a, with the boundaries of selected smooth plains from Denevi et al. (2013). (b) Map of Σ_a, with Mg/Si abundance contours from Weider et al. (2015). Regions in white are unmapped.

two large regions (approximately to −45° to 45°N, −45° to 45°E, and −60° to 60°N, 135° to −135°E, respectively). Although the regions sampled by Lawrence et al. (2010) only partially overlap the area of our measurements, we note that the lower Σ_a region from NS includes the Caloris basin, which our results (Fig. 9) reveal has a Σ_a value of 46 g/cm^2, consistent with the NS value despite the fact that Caloris only partially filled the NS measurement footprint.

The global XRS-derived Mg/Si map (Weider et al., 2015) provides an independent means to characterize geochemically distinct terranes on Mercury's surface. The Mg/Si map was selected for comparison with Σ_a because (1) its coverage of Mercury's surface is nearly complete, and (2) Mg and Σ_a are uncorrelated, making the two quantities essentially orthogonal in the space of geochemical parameters. The lack of correlation between Mg and Σ_a ($R^2 = 0.2$, where R is the correlation coefficient) was established from a reference set of 40 distinct Solar System materials that includes lunar samples (Haskin and Warren, 1991), chondritic and achondritic meteorites (Nittler et al., 2004), and Mercury compositions (Table 2). Following Weider et al. (2015), we applied a slight smoothing to the raw Mg/Si map to reduce possible systematic variability in the XRS measurements. The resulting Mg/Si values exhibit a three-mode distribution that can be divided into low-Mg (Mg/Si < 0.35), intermediate-Mg (0.35 < Mg/Si < 0.6), and high-Mg (Mg/Si > 0.6) regions.

Mg/Si-value contours are shown on the Σ_a map in Fig. 9b. A number of trends are apparent from this map: (1) the highest Σ_a values are found in association with the high-Mg region at mid-equatorial latitudes, as well as with the low-Mg northern region; (2) the lowest Σ_a values are found in the low-Mg interior Caloris plains; and (3) intermediate Σ_a regions generally correspond to intermediate Mg/Si regions. These correlations are also apparent in Fig. 10, in which Σ_a is plotted versus Mg/Si values for each 5° × 5° equal-area pixel. Three distinct "branches" are observed in the data; the branches are labeled "high Σ_a, low Mg/Si," "low Σ_a, low Mg/Si," and "high Σ_a, high Mg/Si" in Fig. 10. The geographic boundaries of the areas that contribute to these branches form the basis for the geochemical terranes we define on Mercury's surface. The "best guess" Σ_a value for each of these terranes is given in Table 3, along with a comparison with the corresponding reference compositions (Table 2). A discussion of each terrane follows.

5.1. Caloris interior plains terrane

The Caloris interior plains (CIP) geochemical terrane corresponds to the mapped region of Mercury's surface with the lowest

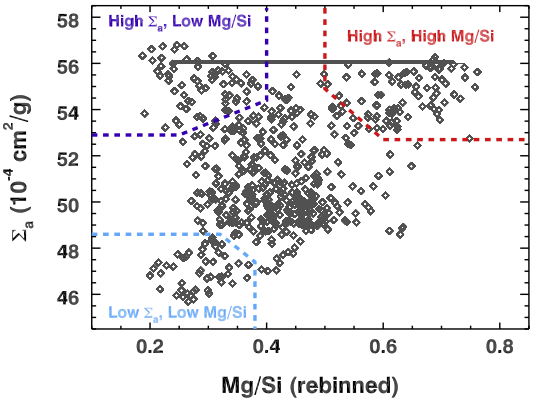

Fig. 10. Σ_a versus Mg/Si values for each 5° × 5° equal-area pixel. Three distinct branches extend from the average values (Section 5.1). As noted in Section 5, Mg is not a dominant contributor to neutron absorption, so the apparent correlations between Σ_a and Mg/Si observed here are related to the geochemistry of Mercury's surface and not the physics of neutron production.

Table 3
Comparison of expected and measured Σ_a values.[a]

ACS-derived Σ_a				Calculated Σ_a		Difference[b]
Terrane	Min.	Max.	Mean	Composition[c]	Value	
Caloris interior plains	45.7	48.7	47.0	CBC	41.3	−5.7
Northern	53.9	56.8	55.9	NC	55.9	0[d]
High-Mg	52.8	56.3	54.8	HMC	41.3	−13.5
Intermediate	45.7	56.8	53.0	IC	40.0	−13.0

[a] All Σ_a values are reported in units of 10^{-4} cm^2/g.
[b] Derived from calculated Σ_a value less the mean ACS-derived value, assuming the "best guess" value of 51.3×10^{-4} cm^2/g.
[c] See Table 2.
[d] The normalization (Σ_a^0) was derived to zero this value.

neutron absorption values ($\delta\Sigma_a < -3 \times 10^{-4}$ cm^2/g; estimated $\Sigma_a < 48.7 \times 10^{-4}$ cm^2/g) and low Mg/Si values (<0.38). The CIP terrane (Fig. 11) is spatially confined to the smooth plains interior to the 1550-km-diameter Caloris basin (Denevi et al., 2009, 2013), except in the northeastern corner of Caloris where the terrane extends beyond the basin. Caloris is the youngest large impact basin on Mercury's surface (Murchie et al., 2008; Fassett et al., 2012). Compared with the planetary mean (Robinson et al., 2008; Denevi et al., 2009), the interior smooth plains have ~10% higher reflectance and a slightly steeper, or "redder," slope in the wavelength range. These differences in reflectance and color for the interior smooth plains are evidence for formation via post-impact volcanism, rather than emplacement as an impact melt (Murchie et al., 2008; Denevi et al., 2009). Additional evidence for a volcanic origin includes the presence of centers of pyroclastic volcanism along the basin rim (Murchie et al., 2008; Head et al., 2008) and a density of impact craters less than that of the basin rim and ejecta interior (Fassett et al., 2009; Denevi et al., 2013). The spatial scale of our geochemical mapping is insensitive to the small exposures of low-reflectance material (LRM)—likely Caloris impact melt material (Ernst et al., 2015)—that have been excavated by impact craters within the interior plains.

The distinctive composition of the Caloris interior plains, as suggested by their color and reflectance properties, is supported by XRS measurements demonstrating that they consist of material with lower Mg/Si, S/Si, Ca/Si, and Fe/Si, and higher Al/Si ratios than the planetary averages (Weider et al., 2015). That the CIP terrane is almost entirely contained within the boundaries of the interior plains supports the hypothesis of a distinct composition and possibly a different origin for the spectrally distinct interior and exterior plains units (Fassett et al., 2009; Denevi et al., 2013).

We used XRS measurements of the CIP area (Weider et al., 2014, 2015), coupled with the low Na/Si and Cl/Si abundances found for equatorial regions from GRS (Peplowski et al., 2014; Evans et al., 2014), to create the CBC composition given in Table 2. Σ_a of the CBC is 43.1×10^{-4} cm^2/g, which is 5.7×10^{-4} cm^2/g lower than the mean GRS-derived value for the region (Table 3). This comparison suggests that the CIP may contain unidentified neutron-absorbing elements, although substantially less (by weight fraction) than other geochemical terranes (see Table 3).

The CIP signature, which includes the lowest Σ_a values seen on the surface, does not appear anywhere else in the mapped region at the ~1000 km horizontal scale of the Σ_a measurements. The uniqueness of the CIP terrane indicates that the elemental composition of the CIP, particularly for those elements that control the neutron measurements, is not widely matched in Mercury's northern hemisphere. Our findings suggest that the composition of the CIP is substantially different from that of the northern volcanic plains (Section 5.2), despite the spectral similarities of the two regions (Denevi et al., 2013). Therefore, we propose the CIP

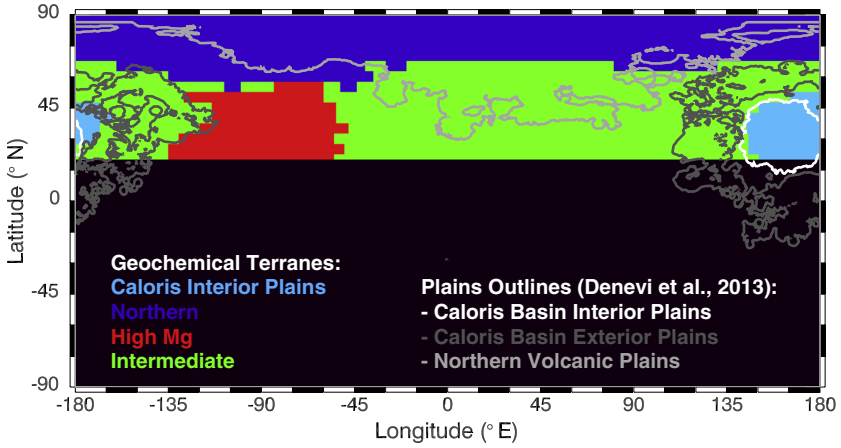

Fig. 11. The major geochemical terranes in Mercury's northern hemisphere. The terranes are color coded by Mg/Si and Σ_a values, as defined in Fig. 10 (Section 5.1). Regions in black are unmapped.

were derived from magmas that originated from a source region distinct from that of the other volcanic deposits in Mercury's northern hemisphere. If the CIP is the result of magmatism triggered by impact-induced heating and convection (Roberts and Barnouin, 2012), the Caloris-forming event may have sampled a volume of the mantle that did not contribute to the magmas that formed the other plains units. The Caloris basin may therefore constitute a window into the vertical and/or horizontal heterogeneity of Mercury's mantle, as has also been proposed by Weider et al. (2015).

5.2. Northern terrane

The northern geochemical terrane defined here corresponds to the region of Mercury's surface with the highest mapped neutron absorption values ($\delta\Sigma_a > 1.5 \times 10^{-4}$ cm^2/g, estimated $\Sigma_a > 53.9 \times 10^{-4}$ cm^2/g) and low Mg/Si values (<~0.4). The spatial extent of the northern terrane (Fig. 11) is generally limited to Mercury's northernmost (>60°N) latitudes. This region is dominated by the northern volcanic plains (NVP) (Head et al., 2011; Denevi et al., 2013), but the boundaries of the NVP do not correspond to those of the northern geochemical terrane (Fig. 11). We note that the northern terrane frequently extends to, but does not cross into, the boundaries of the Caloris basin exterior plains, as shown in Fig. 11. Although the northern terrane does not correspond to a mapped geomorphological unit, it is spatially related to variations in the abundances of other elements that were not used in the definition of geochemical terranes followed here. In particular, the northern terrane corresponds closely to the high-K region (Peplowski et al., 2012), the approximate boundaries of the high-Na region derived from Na/Si variations with latitude (Peplowski et al., 2014), and a regional low in Al/Si ratios (Weider et al., 2015).

We used MESSENGER-derived elemental concentration measurements for high northern latitudes to derive the northern composition (NC, Table 2), which has a mean Σ_a value of 55.9×10^{-4} cm^2/g (Table 3). The mapped Σ_a values for the northern terrane are consistent with those calculated for the NC composition, but the overall normalization of Σ_a values was selected to maintain this correspondence (Section 4.2). This high Σ_a value, relative to values for other MESSENGER-derived compositions (Table 2), is the result of elevated Na/Si (Peplowski et al., 2014) and Cl/Si (Evans et al., 2014) ratios for Mercury's most northern latitudes, as observed by the GRS. Thermal redistribution of Na and Cl, by analogy with K (Peplowski et al., 2012), has been suggested as a possible explanation for the elevated abundances of moderately volatile elements in this region (Peplowski et al., 2014; Evans et al., 2014). However, the observation of low Mg/Si and Al/Si values in the northern terrane (Weider et al., 2015) provides evidence against this hypothesis, as Mg and Al are unlikely to be modified by thermal conditions on the surface.

The northern terrane is the one geochemical unit that may be subject to neutron flux modification by the presence of H (see Section 2.3). We predict that the ACS-measured neutron flux may be lowered by as much as 1% at latitudes >78°N by the H content of the radar-bright polar deposits. This effect would correspond to an increase in Σ_a of $\leqslant 3 \times 10^{-4}$ cm^2/g (Fig. 7). Removing this contribution would modify the mapped Σ_a values of this region (Table 3) from $(53.9–56.8) \times 10^{-4}$ cm^2/g to $(50.9–56.8) \times 10^{-4}$ cm^2/g. This difference allows for possible additional neutron absorbers in the region (Section 5.3). The need for and quantity of such elements, however, depends on the actual magnitude of the contribution from H to the ACS measurements. We note that the northern terrane extends to latitudes that are lower (60°N) than we would expect to be influenced by the polar H deposits (>78°N). It is therefore unlikely that H is the dominant chemical contributor to the measured neuron properties of this unit.

5.3. High-Mg terrane

The high-Mg terrane corresponds to the area of Mercury's surface that has high neutron absorption ($\delta\Sigma_a > 1.4 \times 10^{-4}$ cm^2/g, estimated $\Sigma_a > 51.5 \times 10^{-4}$ cm^2/g) and the highest Mg/Si values (>~0.5). The spatial extent of the high-Mg terrane is strongly correlated with the large (>5×10^6 km^2) high-magnesium region (HMR) identified by Weider et al. (2015) from XRS observations. The western and northern boundaries of the high-Mg terrane closely follow the borders of the younger Caloris exterior plains and northern volcanic plains, respectively (Fig. 11).

Weider et al. (2015) suggested that the distinct chemical signature of the HMR might be the result of early high-degree partial melting, mantle excavation by an unidentified impact basin, and/or magma originating from a chemically distinct volume of the mantle. They also observed that the HMR has relatively thin crust and includes some of Mercury's most heavily cratered areas. Measurements of Al/Si, S/Si, and Ca/Si in this area (Fig. 12) show that the high-Mg terrane has the highest Ca/Si and S/Si content on the mapped portion of Mercury's surface, along with the low Al/Si abundances.

MESSENGER geochemical data acquired within the HMR were used to derive the high-Mg composition (HMC) of Table 2. A

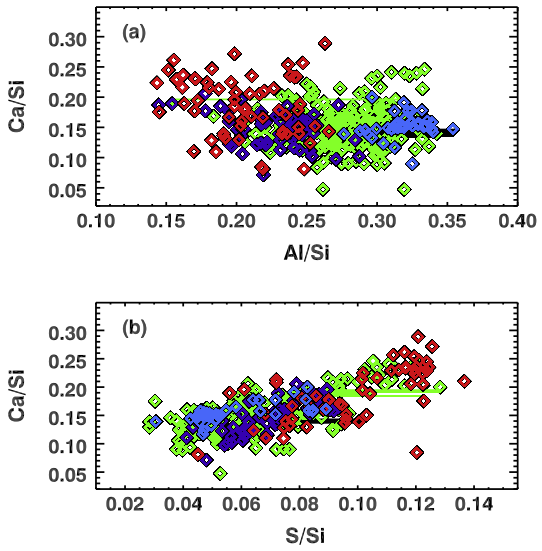

Fig. 12. (a) Ca/Si versus Al/Si and (b) S/Si values color coded by their parent geochemical terrane (Fig. 11). Abundance values were derived from the MESSENGER XRS elemental maps of Weider et al. (2015), re-binned to the 5° × 5° equal-area pixels of Fig. 9.

comparison of the calculated Σ_a value for the HMC and our "best-guess" Σ_a values for the high-Mg terrane, shown in Table 3, highlights the large difference between the expected and measured Σ_a values of $\sim 13 \times 10^{-4}$ cm^2/g. This difference indicates that the elemental composition of the high-Mg terrane is not fully represented by the HMC composition. Specifically, the material of this terrane must contain a substantial abundance of one or more additional neutron-absorbing elements. We consider several possible solutions to this missing-neutron-absorber problem below.

5.3.1. Increased Ti, Cr, and Mn

On the Moon, Σ_a is closely correlated with the Fe and Ti content of surface materials (e.g., Elphic et al., 2000). Although Mercury's surface is markedly depleted in these elements (1 wt% < Fe < 2.5 wt%, Ti < 0.8 wt%) relative to lunar materials (1.7 wt% < Fe < 21.8 wt%, 0.1 wt% < Ti < 6.1 wt%; Prettyman et al., 2006), increased concentrations of these or similar elements in the HMR may be the source of the missing neutron absorption in this region. Recent XRS measurements of the HMR have revealed Fe/Si values of 0.07–0.10 (1.7–2.5 wt% Fe for 25 wt% Si), the highest yet observed on Mercury (Frank et al., 2015). These measurements confirm that at least one of the most typical neutron-absorbing elements is more abundant in the HMR. However, a higher Fe content in the HMR is already included in the HMC composition of Table 2 and thus cannot account for the missing absorption.

A possible solution to the missing-neutron-absorber problem is that the transition metals Ti, Mn, and Cr, are also elevated in the high-Mg terrane. In the absence of elemental concentration maps for these elements, we used global mean values (Ti/Si = 0.012, Cr/Si = 0.005, Mn/Si = 0.004) for each region in our reference compositions (Table 2). Without knowledge of their relative spatial distributions, we assumed that all three elements track together, and we considered the consequence of increasing each by a uniform factor. We iterated this normalization until the Σ_a value of the HMC matched the mean value for the high-Mg terrane. The results, shown in Table 4, indicate that Ti, Mn, and Cr concentrations would need to be increased by a factor of 4.4 relative to our HMC concentrations to account for the missing $\sim 13 \times 10^{-4}$ cm^2/g of absorption. The validity of this hypothesis can be tested with future XRS measurements, but we note that this enhancement is larger than the approximately factor of two increase in Fe concentrations in the HMR relative to the IC (Table 2).

Table 4
Summary of hypotheses to account for elevated Σ_a values in the high-Mg terrane.

Scenario	Element	σ_a[a] (b)	Elemental concentration	
			Reference[b]	Required[c]
High metal concentrations	Ti	5.99	0.29 wt%	1.3 wt%
	Cr	3.04	0.12 wt%	0.5 wt%
	Mn	13.4	0.10 wt%	0.4 wt%
Enrichment in moderately volatile elements	Na	0.528	2.4 wt%	5.6 wt%
	Cl	33.2	0.1 wt%	0.3 wt%
Enrichment in rare-earth elements (REEs)	Sm	10,100	0.9 ppm	9 ppm
	Eu	5660	0 ppm	4 ppm[d]
	Gd	22,800	1.2 ppm	12 ppm
High concentration of solar-wind-implanted H	H	0.33[e]	0 ppm	~300 ppm

[a] Reference values at 0.0253 eV from Chadwick et al. (2011). For REEs, resonances in σ_a invalidate the assumption of uniformly decreasing σ_a values with increasing neutron energy (see Section 2.1). We therefore adopted the effective σ_a values of Prettyman et al. (2013) for Sm, Eu, and Gd.
[b] The reference composition is HMC (see Table 2).
[c] Elemental concentration required to account for missing Σ_a ($\sim 13 \times 10^{-4}$ cm^2/g) in the high-Mg terrane.
[d] Calculated from Sm abundance under the assumption of a mean Solar System Eu/Sm abundance ratio of 0.48.
[e] The effect of hydrogen arises from moderation of the epithermal component of ACS measurements rather than neutron absorption (see Figs. 3 and 4).

5.3.2. Moderate neutron absorbers

GRS measurements have shown that Cl and Na are two of the most important neutron absorbers on Mercury. Moreover, the concentrations of these elements are known to vary across Mercury's surface (Peplowski et al., 2014; Evans et al., 2014). Spatially resolved Na and Cl abundances for the HMC are not available, so we used the mean equatorial values. Following Section 5.3.1, we estimate that a factor of 2.4 increase in the abundance of Cl and Na is required to account for the missing neutron absorption in the high-Mg terrane (Table 4).

The Caloris interior plains are at latitudes comparable to those of the high-magnesium terrane, so the former would need to have lower Na/Si and Cl/Si ratios to maintain the average GRS-measured value at mid and equatorial latitudes. That change would lower the Σ_a value for the CIP from our current estimate of 41.3×10^{-4} cm^2/g, a value that is already lower than the measured values for this region (~ 45.7–48.7×10^{-4} cm^2/g). Although invoking higher Na and Cl is therefore a possible solution to the missing Σ_a value in the high-Mg terrane, such a solution would be problematic for the CIP.

5.3.3. Rare earth elements

The rare earth elements (REEs) Sm, Eu, and Gd have extremely high microscopic neutron-absorption cross sections of 10,100, 4550, and 22,800 barns, respectively. These values are orders of magnitude higher than those of more abundant elements (Table 2), so even minor amounts of these trace elements can cause notable increases to the Σ_a value of the regolith. This phenomenon was noted for the Moon, for which Elphic et al. (2000) used thermal neutron measurements to map Gd and Sm abundances across the lunar surface. The HMC already includes estimates of Gd and Sm abundances derived from the mean northern hemisphere Th concentration and the mean Th/Gd and Th/Sm concentrations for Solar System materials. Elevated REEs in the high-Mg terrane,

beyond the concentrations assumed in Table 2, could provide a possible explanation for the missing neutron absorbers.

Following Sections 5.3.1 and 5.3.2, we estimated the REE abundances required to account for the missing neutron absorbers in the high-Mg terrane by scaling the adopted HMC Gd and Sm values by a single normalization. We have also included Eu by adopting a typical Eu/Sm weight ratio (0.48) for Solar System materials (Lodders and Fegley, 1998). The required normalization, a factor of 10.5, provides total REE abundances of 9 ppm Sm, 4 ppm Eu, and 12 ppm Gd (Table 4) to account for the missing $\sim 13 \times 10^{-4}$ cm^2/g. These concentrations are approximately 50 times those found in CI chondrites (Lodders and Fegley, 1998), a common reference material thought to represent bulk Solar System composition.

This hypothesis of elevated REEs, relative to CI chondrites, in the high-Mg terrane requires a mechanism to concentrate these elements into the surface materials. On the Moon, REEs and other incompatible elements are concentrated in KREEP, a material believed to represent the residue of fractional crystallization of the lunar magma ocean. The high-Mg terrane contains some of the lowest K abundances found in Mercury's northern hemisphere (Peplowski et al., 2012), so a similar process is unlikely to have created an enhancement of REEs in the high-Mg terrane. Another possibility is that the REEs are contained in oldhamite (CaS), a mineral known to be a host of REEs in meteorite samples (Dickinson and McCoy, 1997). The correlation between Ca/Si and S/Si on Mercury (Nittler et al., 2011; Weider et al., 2012) is consistent with the presence of oldhamite on the surface. The highest Ca/Si and S/Si values are observed in the HMR (Fig. 12), which supports the hypothesis that oldhamite, and by extension REEs, are concentrated in the HMR.

Attributing the missing neutron absorbers in the high-Mg region to REEs in oldhamite requires extending this supposition to other regions on Mercury. The other geochemical terranes have S and Ca abundances that are approximately 50% of those found in the high-Mg terrane (Fig. 12), suggesting that these regions have similarly reduced concentrations of oldhamite and, by extension, REE abundances. These regions would therefore be expected to display $\sim 6.5 \times 10^{-4}$ cm^2/g of neutron absorption from REEs. This value is 5–6 times that predicted from our Th-derived Sm and Gd estimates (Table 2) but is consistent with the differences in Σ_a values for the CBC/CIP and IC/intermediate terrane (Table 3), as well as notionally consistent with the difference between the NC and northern terrain when also considering the potential effects of H (Section 5.2). A detailed examination of the relationship between variations in Σ_a and in Ca/Si and S/Si ratios is required to explore further the hypothesis that oldhamite is a major REE carrier on Mercury.

Terrestrial analogs for Mercury surface materials offer another way to examine the likelihood of elevated REEs in the high-Mg region. Given that REEs are highly incompatible during silicate partial melting, we can investigate the extraction of low-degree partial melts from mantle source regions that contain REEs. For instance, mid-ocean ridge basalts (MORBs), which have K/Th ratios similar to those on Mercury (Peplowski et al., 2011, 2012), also have elevated concentrations of REEs (3.5 ppm Sm, 1.3 ppm Eu, 5.1 ppm Gd; Lodders and Fegley, 1998). These values are within a factor of 2–3 of the values that are required to account for the missing neutron absorbers in the high-Mg terrane (Table 3). Weider et al. (2012) showed that terrestrial komatiites are a match to some XRS-derived major element ratios within Mercury's intercrater plains and heavily cratered terrain (IcP/HCT). A large number of the IcP/HCT XRS measurements fall within the high-Mg terrane, so komatiites may constitute an approximate terrestrial analog for materials in the high-Mg terrane. Mean REE concentrations within Gorgona komatiites (1.3 ppm Sm, 0.6 ppm Eu, and 2.3 ppm Gd; Aitken and Echeverria, 1984) are elevated with respect to CI chondrites, but they are still a factor of 5–7 lower than that required to resolve the missing absorption problem on the basis of REEs alone.

5.3.4. Hydrogen

The missing $\sim 13 \times 10^{-4}$ cm^2/g in the high-Mg terrane could be an artifact of the thermal plus epithermal neutron mixture measured by the ACS. In this scenario, the neutron absorption decrease occurs in the epithermal energy range but manifests as an apparent increase in neutron absorption, because of our assumption that all neutron variability at mid-latitudes is attributable to thermal neutrons (Section 2.3). Under this hypothesis, ~300 ppm of H (Fig. 4) in the high-Mg terrane would be required to account for the 3.6% lower count rate in the high-Mg terrane than for intermediate terrane (Section 5.4).

The high-Mg terrane is a mid-latitude to equatorial feature, so H in this region is unlikely to be in the same form as the water ice near the poles (e.g., Lawrence et al., 2013a). The hydrogen might instead take the form of adsorbed H in minerals, e.g., as a result of solar wind implantation. The high-Mg terrane includes some of Mercury's oldest surfaces (Weider et al., 2015) and therefore has had the most time to accumulate solar H. The possibility of elevated H in this region is thus increased. The similarly ancient lunar highlands have a mean hydrogen concentration of 65 ppm and a maximum of 121 ppm (Lawrence et al., 2015), which is lower than the 300 ppm required here. Although the solar wind flux is higher at Mercury, the maximum lunar concentration represents a saturation value (Lawrence et al., 2015) that would presumably be met earlier at Mercury. On the Moon, only fresh (rayed) craters appear to be sufficiently young to contain abundances of solar-wind-implanted H resolvably lower than average. It is therefore unlikely that this hypothesis can account for differences in the neutron properties among our geochemical terranes, which are equivalently old relative to rayed craters.

Alternatively, a H enhancement may originate from the magmatic source region of the high-Mg terrane. Such an effect has been observed in lunar materials. In particular, OH-bearing minerals have been found in association with KREEP-rich materials (e.g., McCubbin et al., 2010; Klima et al., 2013) known to have experienced an unusual magmatic history relative to that of the lunar highlands. The hypothesis that the high-Mg terrane is the manifestation of a distinctive magmatic source region on Mercury (Weider et al., 2015) raises the possibility that high-Mg terrane materials may have incorporated a similarly distinctive H concentration compared with the rest of the surface.

5.4. Intermediate terrane

The intermediate terrane we define has Σ_a and Mg/Si values that do not differ substantially from the planetary averages, i.e., the values do not lie within any of the three regions delineated in Fig. 10. XRS major-element measurements suggest that the intermediate terrane may actually consist of a number of different geochemical terranes that are not apparent in the thermal neutron absorption map (Weider et al., 2015). Despite this complication, we expect that the intermediate terrane generally corresponds to the intermediate composition (IC) of Table 2, which was derived from MESSENGER elemental concentration measurements taken outside of the other geochemical terranes, or from global average values.

Elemental abundance ratios for the intermediate terrane (Fig. 12) indicate that it has generally intermediate values of Ca/Si and S/Si, but Al/Si ratios that are generally higher than in the northern and high-Mg terranes. Only the CIP terrane has higher Al/Si ratios. The intermediate terrane consists mostly of intercrater

terrain (e.g., Whitten et al., 2014), but it also extends into some areas of smooth plains.

As shown in Table 3, our "best guess" Σ_a values are substantially lower than the mean Σ_a value of the intermediate terrane. However, the intermediate terrane has the largest range of Σ_a values, supporting the hypothesis that it consists of several geochemical units that are not resolved in this study. As a result, a detailed examination of any potential missing neutron absorbers for this region is not warranted.

6. Conclusions

Data from MESSENGER's Gamma-Ray Spectrometer anti-coincidence shield have yielded the first maps of neutron absorption across Mercury's surface. These maps have been used to infer the distribution of thermal-neutron-absorbing elements across the planet. This information has been combined with other MESSENGER geochemical measurements to identify and map four distinct geochemical terranes on Mercury. Interpretation of the neutron absorption map and the inferred geochemical terranes leads to the following observations:

- At regional scales, Na, Cl, and Fe are the dominant contributors to observed variability in the concentrations of neutron-absorbing elements on Mercury.
- The Caloris interior plains terrane has a distinct elemental composition, with low Σ_a, Fe/Si, and Mg/Si, as well as high Al/Si. The boundaries of this terrane are generally consistent with the geomorphological boundaries of the Caloris interior smooth plains. A small difference between the expected and measured Σ_a values suggests that this region may host unidentified neutron-absorbing elements.
- The northern geochemical terrane is found at high northern latitudes and corresponds to a region with high Σ_a, Na/Si, Cl/Si, and K abundances, intermediate–to-low Al/Si content, and low Mg/Si abundances.
- The Σ_a value, Al/Si ratio, and K content of the northern terrane differ from those of the Caloris interior plains, indicating different elemental compositions. We suggest that the source magmas for these two volcanic units therefore originated from portions of the mantle with different compositions.
- The boundaries of the northern terrane do not match the boundaries of the northern volcanic plains (NVP). The NVP include areas within both the northern terrane and the intermediate terrane. This finding is consistent with other maps of Mg/Si, Al/Si, and K abundances and demonstrates that the NVP are not a compositionally homogenous unit.
- The high-Mg terrane, which has high Σ_a values and the highest Mg/Si content on the planet, closely corresponds to the high-magnesium region (HMR) identified from XRS observations (Weider et al., 2015). The cause of the elevated Σ_a values in this area is due, in part, to elevated Fe/Si content, but Fe cannot account for the full enhancement. Elevated concentrations of other transition metals (Ti, Cr, Mn), moderate absorbers (Na, Cl), rare-earth elements (Gd, Eu, Sm), or H each provide possible explanations.
- The northern and high-Mg terranes closely follow, but do not cross, the boundaries of the Caloris exterior plains. Those plains are part of the intermediate terrane, which has an elemental composition closer to the planetary average than the other geochemical units.

An unexpected result of this analysis is the demonstration that the NVP and the Caloris basin interior plains are geochemically distinct, despite their generally similar reflectance and color characteristics (Denevi et al., 2009, 2013). There is also a lack of correlation between the boundaries of the northern geochemical unit and the northern smooth plains, despite the general uniformity of their morphological and color characteristics. Our observations, together with those of Weider et al. (2015), therefore show that the relations between geological units and geochemical terranes on Mercury are complex. The increasingly detailed geochemical measurements returned by MESSENGER are only now providing sufficient information to provide insights into these relations.

Acknowledgments

We thank the entire MESSENGER team for their invaluable contributions to the development and operation of the spacecraft. We thank Francis McCubbin and an anonymous reviewer for constructive comments on an earlier version of this manuscript. The MESSENGER mission is supported by the NASA Discovery Program under contracts NAS5-97271 to The Johns Hopkins University Applied Physics Laboratory and NASW-00002 to the Carnegie Institution of Washington. LGE, DJL, and LRN acknowledge support from the MESSENGER Participating Scientist Program.

Appendix A. Data reduction methodology

A.1. Introduction

The need to normalize the measured neutron count rate, $C_n(t)$, to a standard viewing geometry so that compositional information can be derived from the ACS measurements is described in Section 3.3. In addition to being sensitive to surface composition, $C_n(t)$ is a function of the following parameters:

- Altitude, h, more conveniently expressed as the solid angle, Ω, subtended by the planet (Section A.3).
- Vertical velocity, calculated from the time derivative of the altitude, $\frac{dh}{dt}$.
- Spacecraft attitude as expressed by the angle between the detector boresight vector and the spacecraft-to-planet nadir vector (θ), and the angle that measures the rotation of the spacecraft about the nadir vector (ϕ).
- Components of the spacecraft velocity, $\mathbf{V}$, in the spacecraft coordinate frame (x, y, z).
- Local GCR flux, as sampled by the NS triple-coincidence counter, C_T.

In this appendix we detail the empirical corrections that are applied to $C_n(t)$ to remove these sources of variability. Corrections are performed in decreasing order of importance, and some are multivariate in nature, as a result of interdependencies in the sources of variability. The resulting time series of neutron count rates, normalized to our reference geometry, contains information on Mercury's surface composition. Corrections are derived and tested on modeled neutron count rates (Section A.2), which serve as a guide to the normalization process.

A.2. Step 1: Model creation and normalization

We produced modeled neutron count rates for the entire ACS dataset, building on techniques developed for analysis of NS data (Lawrence et al., 2010, 2013a). Additions were made to incorporate the ACS detector and its response to neutrons. The MESSENGER ephemeris was included in the neutron model on a spectrum-by-spectrum basis. In the model we used these inputs to simulate

GCR-induced neutron production within Mercury's regolith (e.g., McKinney et al., 2006), neutron interactions in the regolith as they travel to the surface, neutron transport to the ACS (Feldman et al., 1989), and neutron detection by the ACS (e.g., Fig. 2a). The models accurately reproduced the observed variability arising from systematic effects, such as variable spacecraft altitude and attitude-dependent detector response (Fig. 5). The model accounts for the ACS disk and annulus count rates separately, and as was the case for the data, we limited our analysis to the annulus events (Section 2.2). Models were carried out for multiple surface compositions (Table 1), under the assumption of compositional homogeneity across the surface. A perfectly corrected model, with all systematic variability removed, would thus produce a uniform neutron count rate map for Mercury's surface. This assumption facilitates the use of the models as a test bed for checking the validity of count-rate corrections prior to applying them to the data.

Our first step in the count-rate corrections was to normalize the modeled count-rate time series to the measured count-rate time series. A least-squares minimization routine was used to derive the optimum values for a linear correction to the raw modeled count rates to match the measurements. The resulting normalization,

$$C_n = 0.41\ C_n\ (\text{raw}) - 3.08, \tag{A1}$$

indicates that the simulations overestimate the annulus-measured neutron count rates by a factor of 1/0.41 = 2.44. The most likely sources of this discrepancy are differences between the modeled and actual GCR flux and/or differences in the modeled and actual response of the ACS. For example, the light output of the BC454 scintillator is not included in the simulations and can introduce an efficiency loss to the system. The offset (−3.08) is attributed to imperfect removal of the high-altitude backgrounds from the ACS spectra (Section 3.2).

A.3. Step 2: Solid angle and vertical Doppler correction

The dominant source of variability in the modeled and measured count rates is the altitude of the spacecraft about Mercury (Fig. 5a). This relationship is more conveniently expressed in terms of the fractional solid angle (Ω), the portion of the GRS/ACS 4π-sr field of view that is subtended by Mercury. Ω is calculated from

$$\Omega(h) = \frac{1 - \cos(\theta_{\max})}{2} \tag{A2}$$

where h is the spacecraft altitude and $\theta_{\max}$ is the angle from the sub-nadir point to the horizon. $\theta_{\max}$ is

$$\theta_{\max}(h) = a\cos\left[\frac{[(R_M + h)^2 - R_M^2]^{1/2}}{(R_M + h)}\right], \tag{A3}$$

where R_M is the radius of Mercury (2440 km).

The relationship between thermal neutron count rates and the solid angle is complicated by a second-order effect originating from Doppler enhancement/suppression on the inbound/outbound portions of MESSENGER's orbit (e.g., Feldman and Drake, 1986). The result is a double-valued function for the count rate versus solid angle. This effect prohibits a simple correction based on count rate versus solid angle (e.g., Peplowski et al., 2012). We resolved this ambiguity by performing an empirical correction to the data as a function of both Ω and $\frac{dh}{dt}$. First, the $C_n(t)$ was recast as a function of Ω and $\frac{dh}{dt}$ as

$$C_n(t) \rightarrow C_n\left(\Omega, \frac{dh}{dt}\right). \tag{A4}$$

Our reference geometry specifies normalizing to the average value at an altitude of 1000 km (Ω_0 = 0.15). Averaging between the inbound (dh/dt < 0) and outbound (dh/dt > 0) portions of the orbit effectively normalizes the data to a vertical velocity of 0 km s^{-1}. The normalized count rate $C'_n\left(\Omega, \frac{dh}{dt}\right)$ may be calculated as

$$C'_n\left(\Omega, \frac{dh}{dt}\right) = C_n\left(\Omega, \frac{dh}{dt}\right) \times \left[N_1\left(\Omega_0, \Omega, \frac{dh}{dt}\right)\right]^{-1}, \tag{A5}$$

where the normalization N_1 is shown in Fig. A1. $C'_n\left(\Omega, \frac{dh}{dt}\right)$ was recast back to a normalized count-rate time series, $C'_n(t)$, for which the systematic dependence on altitude and vertical velocity has been removed.

A.4. Step 3: Galactic cosmic ray correction

Neutrons are produced on Mercury via interactions between GCRs and the regolith (Section 2.1). Changes in the surface-incident GCR flux therefore result in changes in the magnitude of the neutron flux from the surface. The NS triple-coincidence count rate (C_T) is a GCR proxy (Feldman et al., 2010; Lawrence et al., 2013a) that was used to remove this effect empirically. $C'_n(t)$ is plotted as a function of C_T in Fig. A2. We re-binned the $C'_n(t)$ measurements into bins of C_T, fit a linear relationship between $C'_n(t)$ and C_T (Fig. A2), de-trended the data, and normalized to a reference C_T value of 26.5 counts s^{-1}. These steps yielded a new time series, $C''_n(t)$, for which the systematic dependence on altitude, vertical velocity, and GCR conditions have been removed. Since the neutron model is predicated on a uniform GCR flux throughout the mission, it does not require this correction.

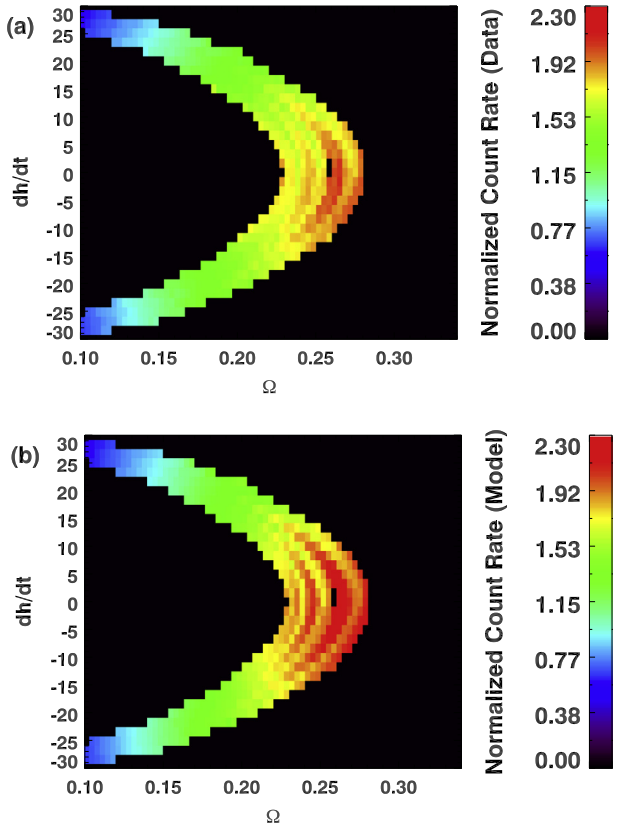

Fig. A1. Neutron count rates for (a) the data and (b) the model as functions of solid angle (Ω) and vertical velocity (dh/dt, in units of km per 20 s). Values are normalized to the mean value at the reference geometry, h = 1000 km (Ω = 0.15).

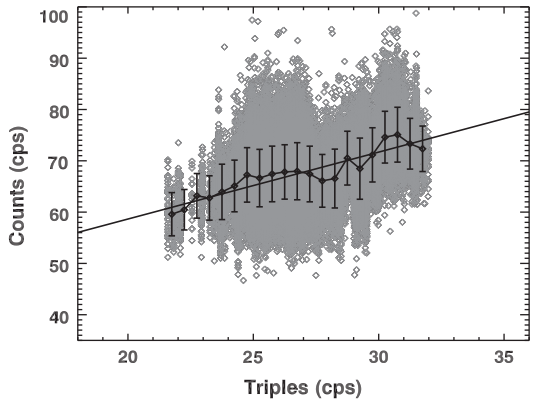

Fig. A2. Measured neutron count rate, after altitude and dh/dt corrections, versus the NS triple-coincidence count-rate (triples) value, a proxy for galactic cosmic ray flux. Raw data (gray) are re-binned by triple value (black points, error bars), and a linear fit to the rebinned values is shown (black line).

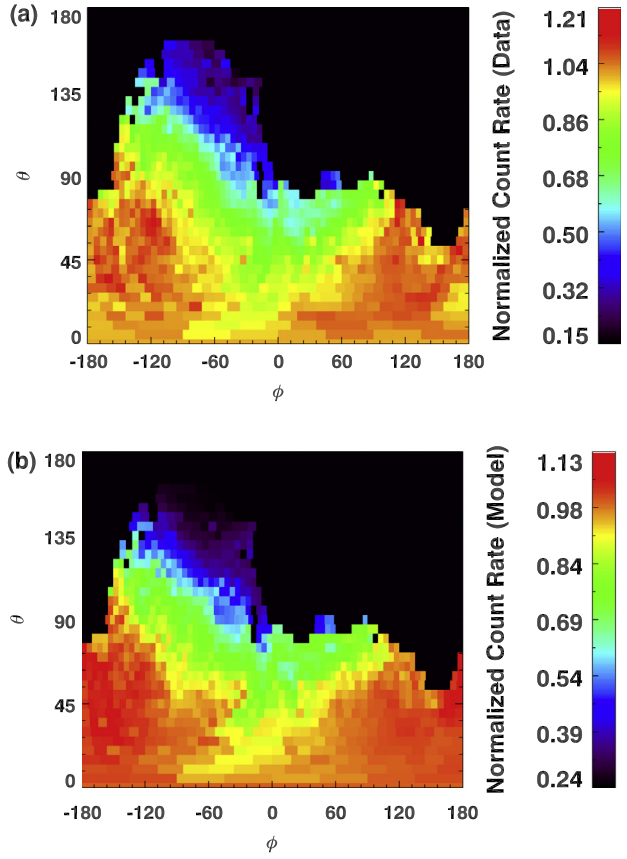

Fig. A3. Neutron count rates for (a) the data and (b) the model as functions of spacecraft attitude (see Section A.5). Values are normalized to the mean value at the reference geometry, $\theta = 0°$.

A.5. Step 4: Detector response correction

The quantity $C''_n(t)$ strongly varies as a function of the detector orientation, relative to Mercury (e.g., Fig. 5b). This effect is the result of neutron transmission losses through ACS-surrounding spacecraft components, e.g., the spacecraft adapter ring and sunshade (Leary et al., 2007; Goldsten et al., 2007), as well as axial asymmetries in the detector volume. We express the GRS attitude in terms of the angles θ and ϕ (see Section A.1 and Peplowski et al., 2012). We recast $C''_n(t)$ as a function of θ and ϕ for both the measured and modeled datasets. Following the procedure detailed in Section A.3, we normalized $C''_n(t)$ to the reference θ value ($\theta_0 = 0°$) as

$$C'''_n(\theta,\phi) = C''_n(\theta,\phi) \times [N_2(\theta_0,\theta,\phi)]^{-1}, \quad \text{(A6)}$$

where N_2 is the normalization shown in Fig. A3. Note that ϕ is unspecified at $\theta = 0°$ and is therefore not considered in the normalization. We recast $C'''_n(\theta,\varphi)$ as a new time series $C'''_n(t)$ for which the systematic dependences on altitude, vertical velocity, local GCR conditions, and spacecraft attitude have been removed.

A.6. Step 5: Minor corrections

Steps 1 through 4 remove the majority of the systematic variability from the neutron time series, but weak correlations between $C'''_n(t)$ and V_x, V_z are still observed. The V_x dependence, which originates from the non-isotropic response of the detector, partially mimics the Doppler filter technique used by the NS to segregate thermal and epithermal neutrons in the lithium glass detectors. Following the procedures used in steps 2 and 4, $C'''_n(t)$ was plotted as a function of V_x and V_z, and empirically corrected to reference V_x and V_z values of zero. Because of the small magnitude of these corrections, we have omitted inclusion of the details of these corrections.

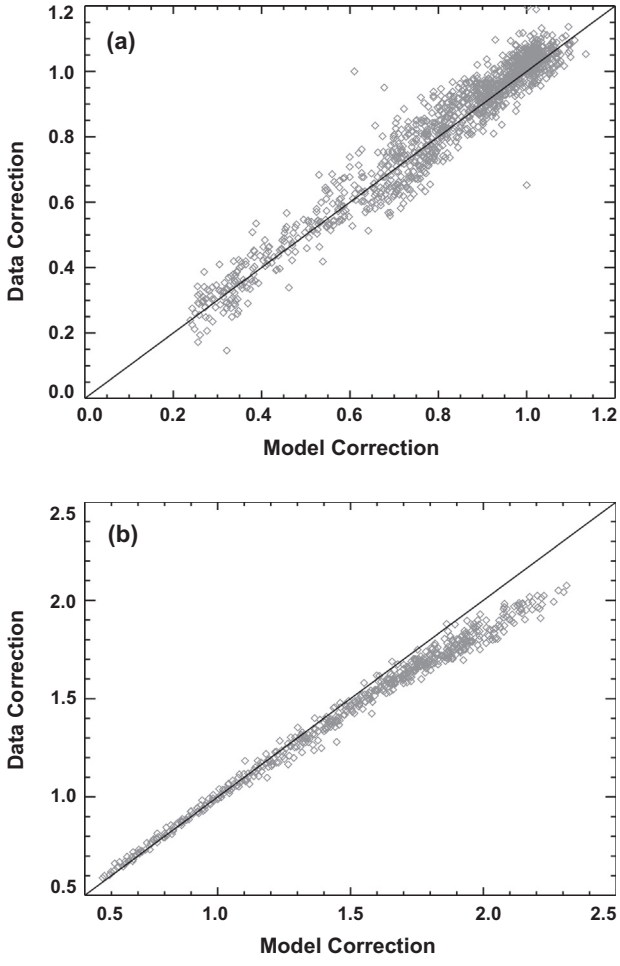

Fig. A4. Data versus model normalization factors for the (a) detector response and (b) altitude corrections. The black line is the 1:1 line expected if the normalizations were identical.

A.7. Application of the corrections

Although this appendix details the model and measurement corrections as parallel steps, in practice this procedure was performed first for the model. The order and nature of the corrections were iterated with the goal of creating a nearly uniform model count-rate map (Section A.2). Once the correction procedure was optimized, it was then applied to the dataset. The corrections themselves were developed independently for the modeled and measured neutron count rates, and in general there was excellent agreement between the two. The correction factors for the model versus those for the measurements for steps 2 and 4 are plotted in Fig. A4. For the detector response (Fig. A4a), the two corrections plot along the 1:1 line expected if the two corrections are essentially identical. This result indicates that the normalized simulations successfully reproduced the response of the ACS.

A different situation is observed for the Ω corrections (Fig. A4b). For these values, the corrections are similar near the reference altitude (Ω = 0.15), where the correction is ~1:1, but they diverge at large (>1.5) values. This discrepancy, which occurs over Mercury's high northern latitudes, results from degeneracies between Mercury's surface composition and MESSENGER's orbit. During the timeframe of the reported ACS measurements, MESSENGER's altitude decreased systematically with increasing latitude. As a result, latitude-dependent variations in surface composition trade off with altitude-induced variations in signal intensity. Even before this work, Mercury's north polar region was known to be compositionally distinct in terms of Mg/Si, Al/Si (Weider et al., 2012, 2015), K (Peplowski et al., 2012), Na/Si (Peplowski et al., 2014), and Cl/Si (Evans et al., 2014). In particular, the presence of elevated Na and Cl raises neutron absorption in this region, a phenomenon that can account for the divergence in the corrections since the model is for a homogenous surface composition. These observations led us to apply the model-derived N_1 correction to the data for the $C_n(\Omega, \frac{dh}{dt})$ correction. This step is required to avoid removing a compositional signal from the data during the correction process.

References

Agostinelli, S. et al., 2003. GEANT4-A simulation toolkit. Nucl. Instrum. Meth. Phys. Res. A 506, 250–303, http://dx.doi.org/10.1016/S0168-9002(03)01368-8.

Aitken, B.G., Echeverria, L.M., 1984. Petrology and geochemistry of komatiites and tholeiites from Gorgona Island, Colombia. Contrib. Mineral. Petrol. 86, 94–105.

Chabot, N.L. et al., 2014. Images of surface volatiles in Mercury's polar craters acquired by the MESSENGER spacecraft. Geology 42, 1051–1054.

Chadwick, M.B. et al., 2011. ENDF/B-VII.1 nuclear data for science and technology: Cross sections, covariances, fission product yields and decay data. Nuclear Data Sheets 112, 2887–2996, http://dx.doi.org/10.1016/j.nds.2011.11.002.

Denevi, B.W. et al., 2009. The evolution of Mercury's crust: A global perspective from MESSENGER. Science 324, 613–618, http://dx.doi.org/10.1126/science.1172226.

Denevi, B.W. et al., 2013. The distribution and origin of smooth plains on Mercury. J. Geophys. Res. Planets 118, 891–907, http://dx.doi.org/10.1002/jgre.20075.

Dickinson, T.L., McCoy, T.J., 1997. Experimental rare-earth-element partitioning in oldhamite: Implications for the igneous origin of aubritic oldhamite. Meteorit. Planet. Sci. 32, 395–412, http://dx.doi.org/10.1111/j.1945=5100.1997.tb01283.x.

Elphic, R.C. et al., 2000. Lunar rare earth element distribution and ramifications for FeO and TiO_2: Lunar Prospector neutron spectrometer observations. J. Geophys. Res. 105, 20333–20345, http://dx.doi.org/10.1029/1999JE001176.

Ernst, C.M. et al., 2015–2014. Stratigraphy of the Caloris basin: Implications for volcanic history and basin impact melt. Icarus, 250, 413–429 http://dx.doi.org//10.1016/j.icarus.2014.11.003.

Evans, L.G. et al., 2012. Major-element abundances on the surface of Mercury: Results from the MESSENGER Gamma-Ray Spectrometer. J. Geophys. Res. 117, E00L07, http://dx.doi.org/10.1029/2012JE004178.

Evans, L.G. et al., 2014. Chlorine on the surface of Mercury: Implications for Mercury's surface evolution. Lunar Planet. Sci. 45. Abstract 1794.

Fassett, C.I. et al., 2009. Caloris impact basin: Exterior geomorphology, stratigraphy, morphometry, radial sculpture, and smooth plains deposits. Earth Planet. Sci. Lett. 285, 297–308, http://dx.doi.org/10.1016/j.epsl.2009.05.022.

Fassett, C.I. et al., 2012. Large impact basins on Mercury: Global distribution, characteristics, and modification history from MESSENGER orbital data. J. Geophys. Res. 117, E00L08, http://dx.doi.org/10.1029/2012JE004154.

Feldman, W.C. et al., 1989. Gravitational effects on planetary neutron flux spectra. J. Geophys. Res. 94, 513–525.

Feldman, W.C. et al., 2000. Chemical information content of lunar thermal and epithermal neutrons. J. Geophys. Res. 105, 20347–20363.

Feldman, W.C. et al., 2010. Evidence for extended acceleration of solar flare ions from 1–8 MeV solar neutrons detected with the MESSENGER Neutron Spectrometer. J. Geophys. Res. 115, A01102, http://dx.doi.org/10.1029/2009JA014535.

Feldman, W.C., Drake, D.M., 1986. A Doppler filter technique to measure the hydrogen content of planetary surfaces. Nucl. Instrum. Meth., Sect. A 245, 182–190.

Frank, E.A. et al., 2015. High-resolution measurements of Mercury's surface composition with the MESSENGER X-Ray Spectrometer. Lunar Planet. Sci., 46, Abstract 1949

Gasnault, O. et al., 2001. Composition from fast neutrons: Application to the Moon. Geophys. Res. Lett. 28, 3797–3800.

Genetay, I. et al., 2003. Elemental content from 0 to 500 keV neutrons: Lunar Prospector results. Planet. Space Sci. 51, 271–280.

Goldsten, J.O. et al., 2007. The MESSENGER Gamma-Ray and Neutron Spectrometer. Space Sci. Rev. 131, 339–391, http://dx.doi.org/10.1007/s11214-007-9262-7.

Harmon, J.K., Slade, M.A., Rice, M.S., 2011. Radar imagery of Mercury's putative polar ice: 1999–2005 Arecibo results. Icarus 211, 37–50, http://dx.doi.org/10.1016/j.icarus.2010.08.007.

Haskin, L., Warren, P., 1991. Lunar chemistry. In: Heiken, G.H., Vaniman, D.T., French, B.M. (Eds.), Lunar Sourcebook: A User's Guide to the Moon. Cambridge Univ. Press, Cambridge, UK, pp. 356–474.

Head, J.W. et al., 2008. Volcanism on Mercury: Evidence from the first MESSENGER flyby. Science 321, 69–72, http://dx.doi.org/10.1126/science.1159256.

Head, J.W. et al., 2011. Flood volcanism in the northern high latitudes of Mercury revealed by MESSENGER. Science 333, 1853–1856, http://dx.dio.ord/10.1126/science.1211997.

Kim, K.J. et al., 2006. Theoretical fluxes of gamma rays from the Martian surface. J. Geophys. Res. 111, E03S09, http://dx.doi.org/10.1029/2005JE002655.

Klima, R. et al., 2013. Remote detection of magmatic water in Bullialdus Crater on the Moon. Nat. Geosci. 6, 737–741. http://dx.doi.org/10.1038/ngeo1909.

Lawrence, D.J. et al., 2010. Identification and measurement of neutron-absorbing elements on Mercury's surface. Icarus 209, 195–200, http://dx.doi.org/10.1016/j.icarus.2010.04.055.

Lawrence, D.J. et al., 2013a. Evidence for water ice near Mercury's north pole from MESSENGER Neutron Spectrometer measurements. Science 339, 292–296, http://dx.doi.org/10.1126/science.1229953.

Lawrence, D.J. et al., 2013b, Characterizing energetic electron events within Mercury's magnetosphere as measured with MESSENGER's Neutron Spectrometer. Presented at 2013 Fall Meeting, Abstract P12B-08, 9–13 December. American Geophysical Union, San Francisco, Calif.

Lawrence, D.J. et al., 2015. Bulk hydrogen abundances in the lunar highlands: Measurements from orbital neutron data. Icarus http://dx.doi.org/10.1016/j.icarus.2015.01.005.

Leary, J.C. et al., 2007. The MESSENGER spacecraft. Space Sci. Rev. 131, 187–217.

Lodders, K., Fegley Jr., B., 1998. In: The Planetary Scientist's Companion. Oxford Univ. Press, New York, NY, p. 319.

Maurice, S. et al., 2004. Reduction of neutron data from Lunar Prospector. J. Geophys. Res. 109, E07S04, http://dx.doi.org/10.1029/2003JE002208.

McCubbin, F.M. et al., 2010. Nominally hydrous magmatism on the Moon. Proc. Natl. Acad. Sci. 107, 11223–11228. http://dx.doi.org/10.1073/pnas.1006677107.

McKinney, G.W. et al., 2006. MCNPX benchmark for cosmic ray interactions with the Moon. J. Geophys. Res. 111, E06004, http://dx.doi.org/10.1029/2005JE002551.

Murchie, S.L. et al., 2008. Geology of the Caloris basin, Mercury: A view from MESSENGER. Science 321, 73–76, http://dx.doi.org/10.1126/science.1159261.

Neumann, G.A. et al., 2013. Bright and dark polar deposits on Mercury: Evidence for surface volatiles. Science 339, 296–300, http://dx.doi.org/10.1126/science.1229764B.

Nittler, L.R. et al., 2004. Bulk elemental compositions of meteorites: A guide for interpreting remote sensing geochemical measurements of planets and asteroids. Antarctic Meteorite Res. 17, 231–251.

Nittler, L.R. et al., 2011. The major-element composition of Mercury's surface from MESSENGER X-ray spectrometry. Science 333, 1847–1850, http://dx.doi.org/10.1126/science.1211567.

Paige, D.A. et al., 2013. Thermal stability of volatiles in the north polar region of Mercury. Science 339, 300–303, http://dx.doi.org/10.1126/science.1231106.

Pelowitz, D.B. (Ed.), 2005. MCNPX user's manual, version 2.5.0, Rep. LA-UR-94-1817. 473 pp., Los Alamos Natl. Lab., Los Alamos, NM.

Peplowski, P.N. et al., 2011. Radioactive elements on Mercury's surface from MESSENGER: Implications for the planet's formation and evolution. Science 333, 1850–1853, http://dx.doi.org/10.1126/science.1211576.

Peplowski, P.N. et al., 2012. Variations in the abundances of potassium and thorium on the surface of Mercury: Results from the MESSENGER Gamma-Ray Spectrometer. J. Geophys. Res. 117, E00L04, http://dx.doi.org/10.1029/1012JE004141.

Peplowski, P.N. et al., 2014. Enhanced sodium abundance in Mercury's north polar region revealed by the MESSENGER Gamma-Ray Spectrometer. Icarus 228, 86–95, http://dx.doi.org/10.1016/j.icarus.2013.09.007.

Prettyman, T.H. et al., 2006. Elemental composition of the lunar surface: Analysis of gamma ray spectroscopy data from Lunar Prospector. J. Geophys. Res. 111, E12007, http://dx.doi.org/10.1029/2005JE002656.

Prettyman, T.H. et al., 2012. Elemental mapping by Dawn reveals exogenic H in Vesta's regolith. Science 338, 242–246, http://dx.doi.org/10.1126/science.1225354.

Prettyman, T.H. et al., 2013. Neutron absorption constraints on the composition of 4 Vesta. Meteorit. Planet. Sci. 48, 2211–2236, http://dx.doi.org/10.111/maps.12244.

Roberts, J.H., Barnouin, O.S., 2012. The effect of the Caloris impact on the mantle dynamics and volcanism of Mercury. J. Geophys. Res. 117, E02007, http://dx.doi.org/10.1029/2001JE003876.

Robinson, M.S. et al., 2008. Reflectance and color variations on Mercury: Regolith processes and compositional heterogeneity. Science 321, 66–69, http://dx.doi.org/10.1126/science.1160080.

Schlemm II, C.E. et al., 2007. The X-Ray Spectrometer on the MESSENGER spacecraft. Space Sci. Rev. 131, 393–415, http://dx.doi.org/10.1007/s11214-007-9248-5.

Slade, M.A., Butler, B.J., Muhleman, D.O., 1992. Mercury radar imaging: Evidence for polar ice. Science 258, 635–640, http://dx.doi.org/10.1126/science.258.5082.635.

Solomon, S.C. et al., 2007. MESSENGER mission overview. Space Sci. Rev. 131, 3–39, http://dx.doi.org/10.1007/s11214-007-9247-6.

Starr, R.D. et al., 2012. MESSENGER detection of electron-induced X-ray fluorescence from Mercury's surface. J. Geophys. Res. 117, E00L02, http://dx.doi.org/10.1029/2012JE004116.

Stockstill-Cahill, K.R. et al., 2012. Magnesium-rich crustal compositions on Mercury: Implications for magmatism from petrologic modeling. J. Geophys. Res. 117, E00L15, http://dx.doi.org/10.1029/2012JE004140.

Weider, S.Z. et al., 2012. Chemical heterogeneity on Mercury's surface revealed by the MESSENGER X-Ray Spectrometer. J. Geophys. Res. 117, E00L05, http://dx.doi.org/10.1029/2012JE004153.

Weider, S.Z. et al., 2014. Mapping Mercury's surface iron abundance with MESSENGER X-Ray Spectrometer data. Icarus 235, 170–186, http://dx.doi.org/10.1016/j.icarus.2013.03.002.

Weider, S.Z. et al., 2015. Evidence for geochemical terranes on Mercury: Global mapping of major elements with MESSENGER's X-Ray Spectrometer. Earth Planet. Sci. Lett. http://dx.doi.org/10.1016/j.epsl.2015.01.023.

Whitten, J.L. et al., 2014. Intercrater plains on Mercury: Insights into unit definition, characterization, and origin from MESSENGER datasets. Icarus 241, 97–113, http://dx.doi.org/10.1016/j.icarus.2014.06.013.